Remote Sensing Systems for Ocean: A Review (Part 1: Passive Systems)

Meisam Amani , *Senior Member, IEEE*, Arsalan Ghorbanian , Milad Asgarimehr , Bahareh Yekkehkhany , Armin Moghimi , Shuanggen Jin , *Senior Member, IEEE*, Amin Naboureh , Farzane Mohseni, Sahel Mahdavi , and Nasir Farsad Layegh

Abstract—Reliable, accurate, and timely information about oceans is important for many applications, including water resource management, hydrological cycle monitoring, environmental studies, agricultural and ecosystem health applications, economy, and the overall health of the environment. In this regard, remote sensing (RS) systems offer exceptional advantages for mapping and monitoring various oceanographic parameters with acceptable temporal and spatial resolutions over the oceans and coastal areas. So far, different methods have been developed to study oceans using various RS systems. This urges the necessity of having review studies that comprehensively discuss various RS systems, including passive and active sensors, and their advantages and limitations for ocean applications. In this article, the goal is to review most RS systems and approaches that have been worked on marine applications. This review paper is divided into two parts. Part 1 is dedicated to the passive RS systems for ocean studies. As such, four primary passive systems, including optical, thermal infrared radiometers, microwave radiometers, and Global Navigation Satellite Systems, are comprehensively discussed. Additionally, this article summarizes the main passive RS sensors and satellites, which have been utilized for different oceanographic applications. Finally, various oceanographic parameters, which can be retrieved from the data acquired by passive RS systems, along with the corresponding methods, are discussed.

Meisam Amani and Sahel Mahdavi are with the Wood Environment and Infrastructure Solutions, Ottawa, ON K2E 7L5, Canada (e-mail: meisam.amani@woodplc.com; sahel.mahdavi@woodplc.com).

Arsalan Ghorbanian, Armin Moghimi, and Farzane Mohseni are with the Department of Remote Sensing and Photogrammetry, Faculty of Geodesy and Geomatics Engineering, K. N. Toosi University of Technology, Tehran 1996715433, Iran (e-mail: a.ghorbanian@email.kntu.ac.ir; moghimi.armin@gmail.com; farzanemohseni@ymail.com).

Milad Asgarimehr is with the German Research Centre for Geosciences GFZ, 14473 Potsdam, Germany (e-mail: milad.asgarimehr@gfz-potsdam.de).

Bahareh Yekkehkhany is with the Department of Geomatics Engineering, University of Calgary, Calgary, AB T2N 1N4, Canada (e-mail: bahareh.yekkehkhany@ucalgary.ca).

Shuanggen Jin is with the School of Remote Sensing and Geomatics Engineering, Nanjing University of Information Science and Technology, Nanjing 210044, China, and also with the Shanghai Astronomical Observatory, Chinese Academy of Sciences, Shanghai 200030, China (e-mail: sgjin@shao.ac.cn).

Amin Naboureh is with the Research Center for Digital Mountain and Remote Sensing Application, Institute of Mountain Hazards and Environment, Chinese Academy of Sciences, Chengdu 610041, China, and also with the University of Chinese Academy of Sciences, Beijing 100049, China (e-mail: amin.nabore@mails.ucas.ac.cn).

Nasir Farsad Layegh is with the Fugro B. V., 3528 AD Utrecht, The Netherlands (e-mail: n.farsad@fugro.com).

Digital Object Identifier 10.1109/JSTARS.2021.3130789

Index Terms—Aquatic vegetation, bathymetry, coral reef, Global Navigation Satellite Systems (GNSS), ocean chlorophyll, ocean color (OC), ocean current, ocean salinity, ocean satellite observations, oil spill, optical remote sensing (ORS), radiometers, sea ice (SI), ship detection, thermal infrared (TIR), tidal.

I. INTRODUCTION

OCEANs, which contain nearly 97% of Earth's water, provide many benefits to the environment and humans [1]. For example, oceans produce the furthermost oxygen (over 50%) and absorb carbon dioxide much more than the atmosphere (50 times) to balance climate [2]. Furthermore, it is reported that oceans provide over 35% of the food production to humans and animals [2]. The impact of oceans on the hydrological cycle also is significant by contributing to the precipitation system and storing vast amounts of open water [3]. Finally, the role of the ocean economy has been increasing due to its importance for the tourism industry, transportations, and offshore resources [4]. For example, ocean economic activities account for approximately 10% of the national gross domestic product in Iceland [4].

Considering the benefits of ocean environments, it is important to effectively monitor them using advanced technologies. In this regard, different Remote Sensing (RS, see Table I for the list of acronyms) systems provide valuable, consistent, and frequent datasets for various applications over oceans and coastal areas [5]. In fact, the only practical approach to acquiring consistent and frequent data across the global ocean is utilizing RS observations [6]. However, it should be noted that the existence of satellite observations does not obviate the necessity of *in-situ* monitoring approaches [7]. In fact, the conjunction of RS data with the current unprecedented amount of *in-situ* measurements enables the development of more superior methods [8].

Any RS system has two primary components, which are 1) platform and 2) sensor. The platform is a vehicle utilized to deploy the sensor, and the sensor is the device that records data. Each remote sensor measures electromagnetic radiation reflected, emitted, or back/forward scattered from Earth. For instance, RS systems can be generally divided into two groups of passive and active. Since Part 1 of this review paper is about passive RS systems, their descriptions are briefly provided ahead. More details are also provided in Sections II–V.

Passive RS systems record reflected electromagnetic energy in the visible, near infrared (NIR), and shortwave infrared (SWIR) bands, as well as emitted electromagnetic energy in the thermal

TABLE I
ACRONYMS AND CORRESPONDING DESCRIPTIONS

1	Advanced Along-Track Scanning Radiometer	AATSR
2	Advanced Baseline Imager	ABI
3	Advanced Microwave Scanning Radiometer	AMSR
4	Advanced Spaceborne Thermal Emission and Reflection Radiometer	ASTER
5	Advanced Very High Resolution Radiometer 3	AVHRR3
6	Brightness Temperature	BT
7	Challenging Minisatellite Payload	CHAMP
8	Chlorophyll	Chl
9	Colored Dissolved Organic Matter	CDOM
10	Conical Microwave Imagery and Sounder	CMIS
11	Cyclone Global Navigation Satellite System	CYGNSS
12	Defense Meteorological Satellite Program	DMSP
13	delay-Doppler Maps	DDMs
14	Dissolved Inorganic Matter	DIM
15	Dissolved Organic Carbon	DOC
16	Electrically Scanning Microwave Radiometer	ESMR
17	European Space Agency	ESA
18	Geostationary Operational Environmental Satellite	OES
19	Global Navigation Satellite Systems	GNSS
20	Global Positioning System	GPS
21	GNSS Reflectometry	GNSS-R
22	GNSS Transpolar Earth Reflectometry exploriNg system	G-TERN
23	GNSS-R, Radio Occultation, and Scatterometry onboard the International Space Station	GEROS-ISS
24	Google Earth Engine	GEE
25	GPS Receiver Remote Sensing Instrument	SGR-ReSI
26	Inherent Optical Properties	IOPs
27	Integrated Program Office	IPO
28	interferometric GNSS-R	iGNSS-R
29	International Ocean Color Coordinating Groupe	IOCCG
30	Low Earth Orbit	LEO
31	Light Detection and Ranging	LiDAR
32	Meteorological Operational Satellite Program of Europe	Metop
33	Microwave Imaging Radiometer using Aperture Synthesis	MIRAS
34	Ministry of Economy, Trade and Industry	METI
35	Moderate Resolution Imaging Spectroradiometer	MODIS
36	MultiSpectral Instrument	MSI
37	National Aeronautics and Space Administration	NASA
38	National Oceanic and Atmospheric Administration	NOAA
39	National Polar-orbiting Operational Environmental Satellite System	NPOESS
40	Naval Research Laboratory	NRL
41	Near Infrared	NIR
42	Near Real Time	NRT
43	Normalized Difference Sea Ice Information Index	NDSII
44	Ocean and Land Colour Instrument	OLCI
45	Ocean Color	OC
46	Ocean Color Satellite	OCS
47	Ocean Oil Spill	OOS
48	Ocean Surface Current	OSC
49	Ocean Surface Height	OSH
50	Ocean Surface Salinity	OSS
51	Ocean Surface Wind	OSW
52	Ocean Wave Height	OWH
53	Operational Land Imager	OLI
54	Optical Remote Sensing	ORS
55	Optical Remote Sensing Systems	ORSS
56	Passive Reflectometry and Interferometry Systems	PARIS
57	Radiative Transfer	RT
58	Remote Sensing	RS
59	Remote Sensing Systems	RSS
60	Root Mean Square Errors	RMSEs
61	Scanning Multi-channel Microwave Radiometer	SMMR
62	Sea Ice	SI
63	Sea Surface Temperature	SST
64	Sea-Viewing Wide Field-of-View Sensor	SeaWiF
65	Shortwave Infrared	SWIR
66	Signal-to-Noise Ratio	SNR
67	Soil Moisture and Ocean Salinity	SMOS
68	Spaceborne Imaging Radar-C	SIR-C
69	Special Sensor Microwave Imager/Sounder	SSMIS
70	Special Sensor Microwave/Imager	SSM/I
71	Stepped Frequency Microwave Radiometer	SFMR
72	Suspended Particulate Matter	SPM
73	Synthetic Aperture Radar	SAR
74	Thermal Infrared	TIR
75	TRMM Microwave Imager	TMI
76	Tropical Rainfall Measuring Mission	TRMM
77	UK Disaster Monitoring Constellation	UK-DM
78	UK-DMC, TechDemoSat-1	TDS-1
79	United States	US
80	United States Geological Survey	USGS
81	Vandenberg Air Force Base	VAFB
82	Sound Navigation and Ranging	SONAR
83	Water-Leaving Reflectance	WLR

TABLE II
CLASSIFICATION OF THE PASSIVE RS SYSTEMS BASED ON THE RANGES OF THE ELECTROMAGNETIC SPECTRUM

RS systems	Wavelength (μm)	Frequency (GHz)
Optical	0.3 - 3	10^5 - 10^6
TIR radiometer	3 - 100	3×10^3 - 10^5
Microwave radiometer	16×10^2 - 3×10^5	1 - 185
GNSS-R	19×10^4 - 25×10^4	1.2 - 1.6

infrared (TIR) and microwave bands. Optical, TIR radiometer, microwave radiometer, and Global Navigation Satellite System Reflectometry (GNSS-R) systems are the main passive RS instruments for oceanographic applications (see Table II).

Various RS systems provide numerous opportunities for studying different oceanographic applications. However, there is not currently a literature review paper that comprehensively discusses the characteristics and applications of different RS systems for oceans. Therefore, in this study, detailed discussions are provided about different RS systems, which can be employed for various ocean studies. To this end, 11 most commonly used RS systems for ocean studies are discussed. Considering the wide range of RS systems for ocean studies, this review paper is divided into two parts. Part 1 discusses four main passive systems through four sections (Sections II–V). In each section, first, a brief introduction of the system and its main characteristics are provided. Then, different systems that have been launched so far or have been planned to launch are discussed. Finally, the oceanographic applications of the systems are briefly explained. It is worth noting that since the main objective of this study is to discuss the characteristics of various RS systems in oceans, the applications are not discussed in detail and several references are provided for each application to read more.

II. OPTICAL RS

Over the past several decades, optical RS systems (ORSS) have been widely used to study the physical, biological, and chemical properties of oceans with cost-effective approaches [9]. For example, the proven feasibility of monitoring oceans by the first Ocean Color Satellite (OCS), Coastal Zone Color Scanner onboard Nimbus-7, launched in 1987 created a unique opportunity to employ OCS data for ocean studies [10], [11]. In this regard, several international organizations, such as the International Ocean Color Coordinating Groupe (IOCCG), were established to provide a principal forum to discuss various aspects and capabilities of ORSS for ocean studies [8], [12].

Water constituents [e.g., Chlorophyll (Chl), particulate organic, and suspended sediments] affect the incident light by absorption, scattering, and attenuation [13]. Consequently, the optical RS (ORS) of the ocean is based on the principle measurement of water-leaving reflectance (WLR) that carries information about the variation of water constituent concentration [11]. Therefore, to exploit ORS data for ocean studies, WLR should be accurately retrieved [14], [15]. To this end, the sun glints and whitecaps' effects should be first removed. It is worth noting that although the sun glints have been mainly considered

as an obstacle in oceanographic applications, multiple studies suggested the applicability of sun glints phenomenon to retrieve several ocean surface parameters, such as wave spectrum and oil slicks [14], [16], [17]. Then, the reflectance values accumulated from the Rayleigh scattering, aerosol scattering, Rayleigh–aerosol interaction, and WLR could be decomposed for further steps [18], [19]. Therefore, it is inevitable to perform atmospheric correction to achieve reliable WLR. Regarding the atmospheric correction, it is possible to remove the Rayleigh scattering contribution by precompiled look-up tables [20]. At the same time, the major uncertainties rely on aerosol scattering and its interactions [21], [22]. It is suggested to use the NIR and SWIR bands for turbid and clear waters, respectively, to reduce and eliminate the effect of aerosol scattering contribution [23], [24]. This concept is based on the assumption that the WLR is zero in these bands, and the possible existing values are recognized because the atmospheric path radiance is related to aerosols [18]. Therefore, it is possible to estimate these values and, subsequently, remove them to minimize the impact of aerosols on WRL. Moreover, to decrease the uncertainties of these methods, it has been recommended to utilize both NIR and SWIR bands in a switching strategy for different water classes that would lead to more accurate results [25]. However, in case of failure of the earlier assumptions, other methodologies were also developed. For instance, the land-oriented atmospheric correction [26], [27] and direct estimation of WLR approaches [28], [29] have also been developed for OCS data atmospheric correction.

Accurate retrieval of WLR is used to estimate the desired ocean water constituents using either empirical or semianalytical approaches [30]. The first approach has a bio-optical basis in which regression or implicit machine learning algorithms are employed. For these models, *in-situ* measurements are usually required for training and validating the RS models [27], [28].

The latter has a bio-geo-optical basis in which the relationship between WLR, inherent optical properties (IOPs), and biochemical constituents are defined through the radiative transfer (RT) models [29], [31].

In summary, the advantages of ORSS for ocean studies are as follows:

1) synoptic coverage with various spatial resolutions;
2) subhourly to daily repeated observations;
3) observations for remote locations that cannot be practically studied using conventional approaches;
4) possibility of near-real-time observations; and
5) long-term and consistent historical observations.

In contrast, there are also several challenges and limitations in utilizing ORS data for oceanographic applications. These are as follows:

1) applying accurate atmospheric correction is challenging, leading to low-quality WLR that may cause significant errors in ocean water constituent retrieval;
2) tidal variation, mainly in coastal and turbid waters, may cause uncertainties;
3) high solar zenith angle values, especially for geostationary satellites, influence the quality of ORS data;

4) ORS observations only provide near-surface water information; and
5) the regional RS models for ocean studies should be tuned using *in-situ* observations.

The global models may have multiple uncertainties due to variation and complexity in turbid and high-water concentrations.

A. Systems

The main requirements for ORSSs are the capability of acquiring images in visible, NIR, and SWIR bands. The first group reflects the concentration of water constituents either by strong or weak absorption [13], and the two others are the most essential to perform atmospheric correction [32]. Other sensor characteristics, such as temporal and spatial resolutions, should also be considered based on the specifications of the study area and the objectives of the project. Table III summarizes important ORSSs. More information about some of these systems is also provided ahead.

The Moderate Resolution Imaging Spectroradiometer (MODIS) sensors were launched into the Earth orbits onboard the Terra and Aqua platforms in 1999 and 2002, respectively. Both sensors capture the whole Earth's surface within 1 to 2 day(s) using 20 spectral bands with spatial resolutions ranging between 250 m and 1000 m. These sensors use whiskbroom scanning technology, and each scene covers a wide swath of approximately 2230 km. So far, many oceanographic products have been provided due to the capability of acquiring MODIS data in many spectral bands [33]. The primary application of MODIS sensors in ocean studies include Chl concentration estimation, colored dissolved organic matter (CDOM) estimation, ocean suspended particulate matter (SPM) estimation, and sea ice (SI) detection and monitoring.

The European Space Agency (ESA) Sentinel-3 (A-B) platforms, carrying the Ocean and Land Colour Instrument (OLCI) sensors, were, respectively, launched in 2016 and 2018 at the height of about 814 km. They provide global coverage within two days with a spatial resolution of 300 m and a swath coverage of 1270 km. OLCI records the Earth's surface in 21 optical bands spreading across the visible to NIR regions of the electromagnetic spectrum. OLCI has been used in many ocean-related studies, such as estimation of the ocean Chl concentration, ocean diffuse attenuation coefficient, and CDOM.

The Operational Land Imager (OLI) is another optical sensor carried by the Landsat-8 satellite providing global Earth observations. Landsat-8 was launched in 2013 as the cooperation between the United States Geological Survey (USGS) and the National Aeronautics and Space Administration (NASA) from the Vandenberg Air Force Base. OLI scenes cover a swath of 185 km with 30-m spatial resolution. This sensor includes nine optical bands ranging from 443 nm to 2300 nm. OLI has been widely used in a variety of applications, including glacier and SI studies.

The Multi-Spectral Instrument (MSI) is a high-resolution optical sensor provided by the ESA, launched by the Sentinel-2 (A-B) in 2015 and 2017. Sentinel-2 has a temporal resolution of

TABLE III
ORSS FOR OCEAN STUDIES

Satellite	Sensor	Temporal resolution	Spatial resolution (m)	Central wavelength (nm)	Time period
SeaStar	SeaWiFS	daily	1100	412 - 865	1997 - 2010
HY-1 A	COCTS	daily	1100	412 - 865	2002 − 2004
HY-1 B	COCTS	daily	1100	412 - 865	2007 − 2013
HY-1 C-D	COCTS	daily	1100	412 - 865	2018 - ongoing
ADEOS	OCTS	daily	700	412 - 865	1996 - 1997
ADEOS	AVNIR	41 days	12, 8	463-820	1996-1997
Beijing-1	BEIJING-1-MS	14 days	32	–	2005-ongoing
CBERS-1/2/2B	HRCC	3-26 days	20	485-830	1999-2010
COMS	GOCI	hourly	500	412 − 865	2011-ongoing
Envisat	MERIS	3 days	300, 1200	412.5 − 900	2002-2012
FCI	MTG	10 min	500, 1000, 2000	444 − 2250	2020-ongoing
GCOM-C	SGLI	2 days	250, 1000	380 − 2210	2018-ongoing
GEO-KOMPSAT-2B	GOCI- II	30 min	250	360 − 900	2020-ongoing
Himawari 8-9	AHI	10 min	500, 1000, 2000	445 − 2260	2015-ongoing
HJ-1 A/B	WVC	4 days	30	430-900	2008-ongoing
IRS 1-6	LISS 1-4	2- 24 days	<1 to 25000	42-1700	1988-ongoing
JPSS 2-4, NOAA 20, SNPP	VIIRS	Daily	375 - 750	412 − 2250	2012-ongoing
Landsat 1-8	MSS, TM, ETM+, OLI, and TIRS	16-18 days	15, 30, 60, 80, 100	412-2215	1972-ongoing
MOS-1	MESSR	17 days	50	51-1100	1987-1996
OceanSat2/3	OCM	2 days	360	412 − 865	2010-ongoing
RapidEye	REIS	> 1 days	6.5	4.75 − 805	2009-ongoing
Sentinel-3A-D	OLCI	2 days	300	400 − 1020	2016-ongoing
Sentinel-2 A/B	MSI	5-10 days	10, 20, 60	443 -2190	2015-ongoing
SPOT 1-5	HRV, HRVIR, and HGR	26 days	2.5, 10, 20	500-1750	1986-ongoing
Terra, Aqua	MODIS	daily	250, 500, 1000	400-14400	2000-ongoing
WorldView 2-3	WV110-WV60	> 3 days	1.84	425-950	2009-ongoing

10 days, while in conjunction, the temporal resolution is reduced to five days. MSI provides optical data in 13 bands with spatial resolutions varying between 10 m and 60 m, and a nominal swath width of 290 km. Capturing several optical bands with relatively higher spatial resolutions has proved MSIs capability in many oceanographic applications, such as glacier studies and IOPs retrieval.

B. Applications

ORS data are employed in many oceanographic applications. These are summarized in Fig. 1 and are discussed in more detail in the following sections.

1) Chlorophyll (Chl): One of the main applications of ORSS is the estimation of Chl concentration [34], [35]. Chl concentration is an essential indicator required to monitor and quantify carbon cycles, food chains, and eutrophication of ocean waters [34]. Therefore, many efforts have been made to generate consistent global Chl products from ORS data (e.g., see Fig. 2). ORSS is a great tool for this application because it provides time-series data over large areas and, thus, allows frequent observations for monitoring the Chl concentration. The retrieval algorithms include simple spectral reflectance rationing and differencing in the clear oceanic water, which leads to the Chl concentration estimations with an uncertainty of approximately 35% [36], [37]. However, the main challenge remains for the turbid waters, which require further assumptions and preprocessing steps to quantify Chl concentration [35]. To tackle this challenge, optical
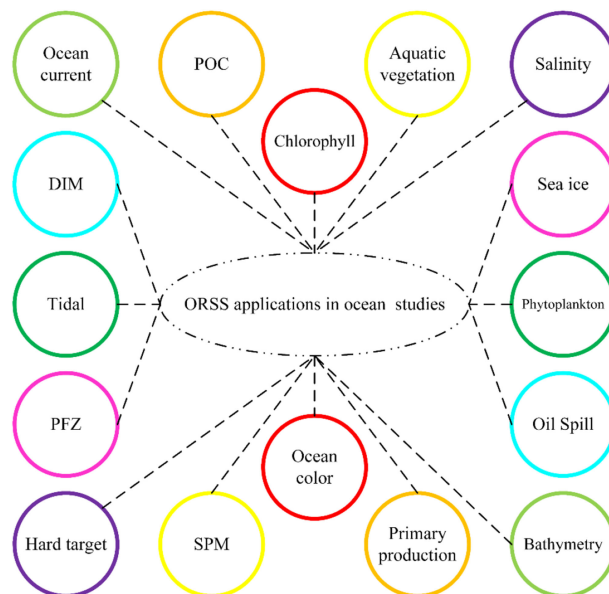

Fig. 1. Main applications of ORSS in ocean studies. POC: Particulate Organic Carbon, SPM: Suspended Particulate Matter, PFZ: Potential Fishing Zone, DIM: Dissolved Inorganic Matter.

water type-based retrieval algorithms have been developed [38]. For instance, Cui *et al.* [34] developed a novel approach based on the global optical water classification method to estimate the Chl
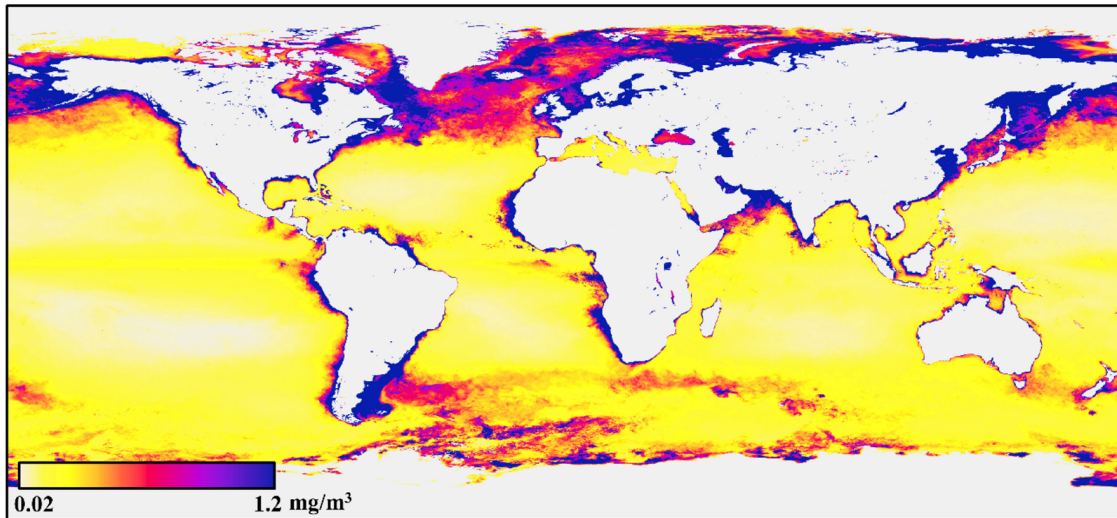
Fig. 2.   Global Chlorophyll (Chl) concentration map generated from the MODIS data in 2016.

concentration in turbid coastal waters [39]. First, they classified the *in-situ* spectral reflectance measurements into different optical water types. Then, nine empirical algorithms were tuned by incorporation of *in-situ* observations using a least-squares linear regression approach. Subsequently, the results were validated using the *in-situ* match-ups technique, in which 17 kernels of 3×3 pixels were employed [40]. Finally, it was reported that all the regionally-tuned empirical algorithms were improved, and the uncertainty of Chl estimation was reduced by approximately 20%.

2) Ocean Color (OC): OC measurements from ORSS provide a synoptic view of the spectral WLR that can be employed to estimate IOPs of the ocean [41], [42]. IOPs reflect oceanic water's scattering and absorption characteristics, which can be utilized to quantify various water constituents. Therefore, many studies have developed numerous algorithms to accurately derive the WLR from the spectral measurements for further applications. This requires highly accurate atmospheric correction algorithms to enable precise retrieval of the WLR values [43].

The OC measurements have been applied to estimate various water constituents, such as oceanic primary productivity [44], carbon stocks [45], dissolved organic carbon (DOC) [46], and Chl concentrations [34]. For instance, Del Castillo and Miller [46] examined the ability of OC measurements to quantify the transport of DOC to the Gulf of Mexico. To this end, *in-situ* data of DOC, CDOM, salinity, and WLR were collected. Afterward, the preprocessing steps were applied, and then, an empirical model was developed to estimate DOC concentrations from the Sea-Viewing Wide Field-of-View Sensor (SeaWiFS) OC ORS data. The empirical model achieved a satisfactory correlation coefficient of about 0.7 when compared with the USGS data.

3) Ocean Surface Salinity (OSS): OSS is a critical indicator of many biogeochemical and physical processes and circulation patterns of coastal and ocean waters [47]. OSS supports studying water constituent alterations and the freshwater and offshore coastal oceanic water mixture. Furthermore, OSS quantification

is an essential element in examining the presence and variation of terrestrial substances and water components, such as inorganic carbon, nutrients, hypoxia, and algal bloom [48]. Conventionally, synoptic and *in-situ* OSS data were collected using ship-based measurements [48]. However, these measurements only provide observations over specific regions, and it is not practical to carry out frequent observations using these methods. Therefore, ORSS is a beneficial and economical approach to estimate OSS due to providing frequent observations over large-scale areas. Linear and nonlinear regression models, as well as machine learning algorithms, are common approaches that have been used for OSS retrieval from the spectral measurements of ORSS. For example, Cui *et al.* [34] considered the inverse relationship between OSS and CDOM concentration to estimate the OSS of the Chinese Bohai Sea. Regarding OSS estimation, four simple band ratios were utilized to develop linear regression models using 75% of *in-situ* measurements. The results showed that the band ratio between 531 nm and 551 nm outperformed others when 25% of *in-situ* data were employed for validation.

4) Ocean Oil Spill (OOS): OOS is a significant environmental problem that endangers the ocean ecosystems through multiple adverse effects [49]. OOS in open waters can be caused due to the ship colliding with obstacles, oil leakage from petroleum tankers, underwater oil pipelines, and technical defects in oil rigs [50]. Despite the primary source of the oil leakage, it is highly required to investigate OOS for further environmental management. In particular, OOS can negatively alter the ocean ecosystem, water quality, and human food chain, as well as bringing economic and environmental damages [51]. Therefore, obtaining reliable information about the location, extent, and movement characteristics of OOS is required to mitigate oil pollution risks and damages. In this regard, ORSS can be an efficient tool because they provide multitemporal observations with broad coverage that can enhance OOS detection and tracking. Spectral information of ORS data can be integrated with image processing techniques and machine learning algorithms

to take the essential information about the OOS. For example, Kompsat-2 high-resolution optical data were employed to detect and map OOS, causing a massive negative impact on the water ecosystem in the Gulf of Mexico in 2010 [52]. To this end, a directional median filter was first adopted to suppress the sun's glint effect caused by the ocean waves. Subsequently, an artificial neural networks model was trained to detect the OOS locations. The method was finally validated based on the receiver operating characteristics and probability of detection methods and obtained 98.12% and 89.56% accuracies, respectively.

5) Ocean Surface Current (OSC): OSC is a critical factor for studying ocean dynamics. The atmospheric-ocean fluxes generate nonuniform buoyancy forcing and wind stress that creates OSC [53]. These phenomena are responsible for large-scale circulations of the ocean water associated with mass transport [54]. OSC is an essential input variable for global climate change studies since it plays a significant role in planetary heat budget calculations [55]. Furthermore, this parameter is required to forecast marine environment interactions and marine navigations. Moreover, OSCs manifest sea life distribution because they affect the migration and movements of fishes to more suitable waters [55].

Recently, several investigations have been devoted to examining the capability of ORSS for OSC studies [56], [57]. For example, Yurovskaya *et al.* [57] introduced a framework to extract the ocean surface water from the multispectral observations using Sentinel-2 images. The cross-spectral analysis was first demonstrated to have a meaningful relationship with ocean surface wave directional characteristics and currents [56]. To this end, they considered the time lag between spectral observations in different wavelengths. Under this condition, the spatiotemporal properties of the OSC vector field can be retrieved from ORS data. Their proposed method was able to estimate the surface wave's speed and direction based on the time lag between different detectors in different bands. The experimental results indicated the promising potential of Sentinel-2 images for OSC studies.

6) Sea Ice (SI): SI is an element of the cryosphere that interchangeably interacts with the ocean and atmosphere. The SI coverage considerably fluctuates within a year. SI monitoring is essential for many environmental applications [58]. Particularly, SI can affect the global climate by altering the surface albedo and reducing solar radiation absorbed by the ocean surface water. Additionally, melting SI, as a freshwater source, changes water constituents and, thus, influences the ocean circulation patterns [58]. SI presence and movement can threaten vessel navigations and impose severe limitations on vessel traffic. Moreover, SI collisions with marine facilities, coastal ports, and oil platforms lead to considerable infrastructure damages [59].

Accordingly, it is essential to have up-to-date information about SI extent and location on the ocean and coastal waters. ORS data can efficiently extract the necessary information about the spatiotemporal distribution of SI [60]. For instance, Su *et al.* [61] employed Sentinel-3 OLCI images to monitor Bohai SI distribution in 2017–2018. First, they evaluated the Normalized Difference Sea Ice Information Index (NDSII) that employed two OLCI bands. Through the validation step, it was observed

that NDSII was affected by the ocean turbidity, which led to moderately low accuracy. Then, the enhanced NDSII was developed by adding two more spectral bands of OLCI to resolve the mentioned drawback. Finally, the proposed index was applied to extract the SI extent of the Bohai Sea, and the results suggested the adequate performance of this approach for SI monitoring in winter.

7) Tidal: Tidal flats are a critical element of the intertidal zone that joins marine and terrestrial ecosystems [62]. They are responsible for shoreline stabilization, storm surge reduction, and wave buffering [63], [64]. They are also highly productive, supplying many biological resources for marine ecosystems [65].

Traditionally, tidal stations were employed to study tidal flats. Although these stations provide highly accurate data, they hinder large-scale studies due to their sparse scattering over ocean environments [62]. Consequently, ORSS were considered for tidal monitoring because of their capabilities in providing time-series and spatially consistent data. For instance, Zhang *et al.* [65] integrated the Landsat-8 images and cloud computing capabilities of Google Earth Engine (GEE) to map tidal areas in China's eastern coasts. Considering the multitemporal requirement for accurate tidal flat mapping, over 1800 Landsat-8 images acquired between 2014 and 2016 were processed in this study. In this regard, a novel multitemporal feature extraction approach and the random forest algorithm were employed. Later, morphological postprocessing was performed to improve the results of the tidal mapping. The proposed approach achieved a significant overall accuracy of about 94.4%, suggesting the beneficial contribution of time-series processing of ORS data for precise tidal mapping.

8) Hard Target: Target detection is a well-known RS application that plays a vital role in accomplishing geospatial information extraction for various tasks [66]. Detecting hard objects, such as ships, oil platforms, and icebergs, is one of the ORSS applications in ocean studies. Object detection allows identifying and tracking moving targets and monitoring their characteristics. For instance, frequent monitoring of oil platforms enables near-real-time OOS detection due to any possible accident [67]. Furthermore, ship/iceberg detection assists regular tracking for safe navigation and environmental studies.

The possibility of providing high-resolution spatial and temporal data made ORSS an attractive choice for hard object detection in coastal and ocean waters. For instance, Li *et al.* [68] proposed a multiscale approach to detect moving and static ships using high-resolution ORS data. The multiscale approach was considered to suppress the limitation of previous methods, which could obtain satisfactory results only on one scale. Thus, they were generally ineffective when applied to multiresolution images. In this regard, an end-to-end network that could detect both inshore and offshore ships was introduced. The proposed algorithm employed regional networks to produce ship candidates using a deep learning algorithm. Subsequently, hierarchical selective filtering was implemented to increase the generality and applicability of the suggested method for different studies. They applied the proposed approach to large ship detection datasets

using ORS data to evaluate its performance. The experimental results showed the high potential of the proposed approach for ship detection in multiscale images.

9) Aquatic Vegetation: Aquatic vegetations are responsible for many ecological cycles in coastal waters. They contribute toward marine carbon sequestration, fisheries and shrimp production, and stabilization [69], [70]. Furthermore, they support marine biodiversity by providing suitable habitats for various marine fauna and protecting the coastal area from seabed erosion [71]. The attributed contributions to aquatic vegetations make them a significantly important element in marine ecosystems. ORSS data can provide regular observations from the marine waters, which can be used for aquatic vegetation studies. These datasets help scientists monitor aquatic vegetations' condition and facilitate progress toward conservation strategies for sustainable development. For instance, Traganos *et al.* [72] employed Sentinel-2 optical data to generate an accurate seagrass map in the Aegean and Ionian Seas. They integrated cloud computing capabilities, optical data, and machine learning algorithms to introduce a framework for large-scale seagrass mapping. First, several preprocessing algorithms, such as cloud masking, atmospheric correction, and singling corrections, were performed on the optical data. These data, along with *in-situ* training samples, were then ingested into a support vector machine algorithm to map the seagrasses over the study area. Later, manual postprocessing was applied to correct miss-classified seagrass polygons. The final overall accuracy, calculated from independent test samples, was 72%. It was finally concluded that the proposed approach provided an ultimately practical workflow for global seagrass monitoring, assisting the climate change studies and coastal management.

10) Bathymetry: Retrieving precise information on bathymetry is a fundamental element for a variety of coastal applications, including navigation, aquaculture management, dredging, and benthic habitats mapping [73]. Furthermore, reliable and frequent bathymetric data can help study the impact of climate change on the environment and determine the potential erosion sites. Vessel-based Sound Navigation and Ranging (SONAR) sensors and airborne Light Detection and Ranging (LiDAR) systems have been widely employed to measure the sea bottom elevation. Although these approaches provide accurate bathymetric measurements, they are resource-intensive and also restricted by access and spatial coverage. However, the ORSS can be efficiently applied to nearshore and shallow water bathymetry due to their frequent observations and wide swath spatial coverage. Accordingly, two common analytical and empirical approaches have been incorporated to derive bathymetric data from the optical data. The first category includes using the RT models for the propagation of light in water, whereas the latter is based on regression analysis between optical reflectance data and *in-situ* observations [74], [75]. For instance, Caballero and Stumpf [73] explored the capability of Sentinel-2 data for high-resolution bathymetric mapping in South Florida, United States (US). To this end, the atmospheric corrections were first applied to produce consistent and reliable WLR. Afterward, several training samples (including bathymetry

data) were extracted from the available digital charts to tune a nonlinear solution based on band rationing [76]. Finally, the independent test samples collected by a LiDAR survey were considered for accuracy assessment. The median absolute errors varied between 0.22 m and 0.5 m over three different regions, indicating the high potential of ORSS data for bathymetric applications.

III. TIR RADIOMETERS

TIR RS systems use the thermal part of the electromagnetic spectrum to derive thermal emission from oceans. The spectral density of radiation emitted by the ocean surface at a specific temperature is determined by Planck's function [77].

$$B_\lambda(T) = 2hc^2\lambda^{-5}\left(e^{hc/(\lambda kT)} - 1\right)^{-1} \tag{1}$$

where T is temperature; h is Planck's constant; c is the speed of light; k is Boltzmann's constant; and λ is the wavelength. This function is specified for ideal emitters. However, natural surfaces emit a ratio of emitted radiance to Planck's function. This ratio is called emissivity and is dependent on the wavelength.

RS systems can operate in various wavelengths, collecting accurate radiance measurements, which are inferred as brightness temperature (BT). Although the BT values are related to one ocean physical variable, known as sea surface temperature (SST), they are not identical because of the absorption, emission, and scattering from the intervening atmosphere [78]. Moreover, very limited, if any, sea surface emission in the TIR spectrum reaches the radiometer in cloudy conditions. Therefore, it is essential to apply cloud masking and atmospheric correction to TIR data [79], [80]. Considering these challenges, the main limitations of employing TIR data are the presence of the cloud and the necessity of an accurate atmospheric correction model [81]. Regarding cloud masking, several methods have been developed based on thresholding [82], Bayes' Theorem [83], and alternating decision tree [84] to identify and mask cloudy pixels. Furthermore, in clear-sky conditions, a substantial portion of the sea surface emission may be interfered with the atmospheric molecules, necessitating performing atmospheric correction to compensate for these issues [79].

There are several main methods for SST retrieval using TIR radiometers data. In this regard, the multichannel strategy is mainly applied to reduce the atmospheric effect on the BT observations and, consequently, to retrieve SST [78]. In this approach, at least two BT observations at wavelengths that are sufficiently sensitive to SST and are differently influenced by the atmosphere are required. Consequently, the atmospheric effect on BT can be linearly approximated by the difference between BTs at two different TIR bands. Moreover, the linearization of Planck's function results in a simpler expression (2) in which the difference of BTs is related to the difference between SST and one BT [85], [86]. Therefore, SST can be calculated from (3)

$$\text{SST} - \text{BT}_i \propto \text{BT}_i - \text{BT}_j \tag{2}$$

$$\text{SST} = a_0 + a_1\text{BT}_i + a_2(\text{BT}_i - \text{BT}_j). \tag{3}$$

TABLE IV
ADVANTAGES AND DISADVANTAGES OF EMPIRICAL AND RT MODELS FOR SST
RETRIEVAL USING THE DATA ACQUIRED BY TIR RADIOMETERS

Factor	Empirical	RT
in-situ data	Required for estimating unknown coefficients through regression analysis.	Not necessary for a well-characterized sensor. However, sensors with low precision calibration require *in-situ* data to tune the offset coefficient.
Sensor calibration	Not necessary because multiple calibration issues are empirically solved by the coefficient determination through regression analysis.	A well-characterized sensor is essential, and in the absence of such a sensor great effort is required for bias correction.
Simplicity of applying	Simple and computationally efficient because these models only use statistical approaches and *in-situ* observations.	More complicated because they require precise RT models for the infrared regions and accurate numerical weather simulations.
Spatiotemporal generality	Can only be precisely matched to the regions where *in-situ* measurements are provided.	The availability of RT models and numerical weather simulations enable high spatiotemporal representativity.

Generally, there are two separate procedures to determine the unknown coefficients (a_0, a_1, and a_2) in (3): 1) empirical and 2) RT models [87]. In empirical methods, the SST values are calculated through a weighted combination of BTs. In fact, the unknown coefficients are determined by applying a regression between BTs and the *in-situ* SST observations [88]. For example, the split window is an empirical method that requires at least two BT values for SST calculation [89]. The split window algorithm is widely used due to its simplicity, computational efficiency, and physically intuitive characteristic [85], [90]. Moreover, various modifications, such as adding more BT values, and nonlinear approaches, were introduced to enhance the performance of the split-window technique [91], [92].

On the other hand, the RT models attempt to determine the unknown coefficients in (3) through numerical simulations of BT measurements [93], [94]. The simulation is driven from the atmospheric profile obtained by radiosondes or numerical weather predictions [95]. The contrasting benefits and limitations of these two approaches for SST retrieval in four aspects are provided in Table IV.

A. Systems

The importance of SST in various applications has motivated the RS community to launch many operational TIR radiometers to acquire BT observations. Moreover, to support long-term and consistent measurements of SST, many programs have been continued by launching new satellites. Table V provides an overview of several TIR radiometers that have contributed, are contributing or will contribute to measuring TIR radiances for SST retrieval. The sensors listed here are among those with principal scientific advancements or are mostly used. Detailed information on some of these systems is provided below.

MODIS instruments were carried by Terra and Aqua satellites and were launched in 1999 and 2002, respectively. Both satellites have a temporal resolution of 1-2 days, and the corresponding sensors record the Earth's surface thermal radiations in 16 TIR bands in both day and night times. These TIR bands reside between 3750 nm and 14235 nm. The spatial resolution of TIR bands is 1 km, and the nominal swath is about 2230 km. Due to the capability to acquire thermal data in several bands, MODIS data were employed for accurate SST retrieval and atmospheric thermal profile. The MODIS SST products have been frequently applied to numerous applications, such as regional weather modeling [96], the thermal stress of corals [97], and cross-shelf circulations [98].

The Advanced Spaceborne Thermal Emission and Reflection Radiometer (ASTER) sensor onboard the Terra platform was launched by the Ministry of Economy, Trade and Industry (METI) of Japan in December 1999. This push broom sensor includes five TIR bands with 90-m spatial resolution, and it can record the Earth's thermal radiation day and night. It supplies a global coverage in 16 days with a scene swath cover of approximately 60 km. ASTER TIR data have been extensively employed for SST retrieval and SI studies.

The Advanced Very High-Resolution Radiometer 3 (AVHRR3) sensors are the third generation of AVHRR instruments, which are mounted on the Meteorological Operational Satellite Program of Europe (Metop) and National Oceanic and Atmospheric Administration (NOAA) satellite series. AVHRR3 and its previous generations were provided by the NOAA. This instrument has three TIR channels centered at 3.74, 10.80, and 12.00 μm. The corresponding TIR images have been mainly applied to SST retrieval and SI studies.

The Advanced Baseline Imager (ABI) is another instrument that replaces the previous generation of IMAGER, carried by a series of Geostationary Operational Environmental Satellite (GOES) satellites. ABI is currently mounted on two GOES-16 and GOES-17 platforms and record the Earth's information using 16 spectral bands. Out of 16 bands, 10 work in the TIR regions ranging from 3.9 to 13.3 μm. ABI captures images with a spatial resolution of 2 km, and as a geostationary satellite, it provides a full field of view every 15 min. GOES-16/17 cover more than half the globe, from the west coast of Africa to New Zealand and from near the Arctic Circle to the Antarctic Circle [99].

B. Applications

TIR radiometers are mainly utilized for SST estimation. SST has a pivotal role in ocean–atmosphere interactions through exchanges of heat, moisture, and momentum [92]. Monitoring SST variability allows achieving a profound perception of climate change [93] and a variety of oceanic currents, such as fronts and eddies [94]. The importance of obtaining reliable SST has led to establishing a group comprising researchers and practitioners collaborating to improve the accuracy and availability of global SST data [95]. Fig. 3 illustrates the global SST products generated from TIR radiometers.

TABLE V
TIR RADIOMETERS FOR OCEAN STUDIES

| Satellite(s)	Sensor	Temporal resolution	Spatial resolution (m)	Central wavelength (nm)	Time period
HY-1 A	COCTS	daily	1100	412 - 865	2002 – 2004
HY-1 B	COCTS	daily	1100	412 - 865	2007 – 2013
HY-1 C-D	COCTS	daily	1100	412 - 865	2018 - ongoing
ERS-1, 2	ATRS 1-2	3 days	1000	370 - 1200	1991 - 2000
Terra, Aqua	MODIS	1-2 days	1000	375 - 1200	1999- ongoing
Envisat	AATSR	1-3 day	1000	375- 1200	2002-2012
GOES 12 - 15	IMAGER	30 min	4000	390 – 1335	2003-ongoing
GOES 16 – 17, GOES T, GOES U	ABI	15 min	2000	39 – 133	2017-ongoing
Himawari 8, 9	AHI	10 min	2000	39 – 133	2015-ongoing
Landsat 4,5,7,8	TIRS	16 day	60,100,120	1080-1200	2013-ongoing
Meteosat 8-11	SEVIRI	15 min	3000	392 – 1340	2004-ongoing
MTG-l1	FCI	10 min	2000	380 – 1330	2022-ogoing
NOAA15-19; MetopA-C	AVHRR3	101 min	1100	374-1200	1998-ongoing
NOAA6; NOAA8; NOAA10; TIROS-N	AVHRR	100 min	1100	374-1100	1979-2001
NOAA7; NOAA9; NOAA11 – 14;	AVHRR2	101 min	1100	374- 1200	1981-2007
Sentinel3 A-D	SLSTR	1 day	1000	374 - 1200	2016-ongoing
Terra	ASTER	16 days	90	830 – 1130	2000-ongoing
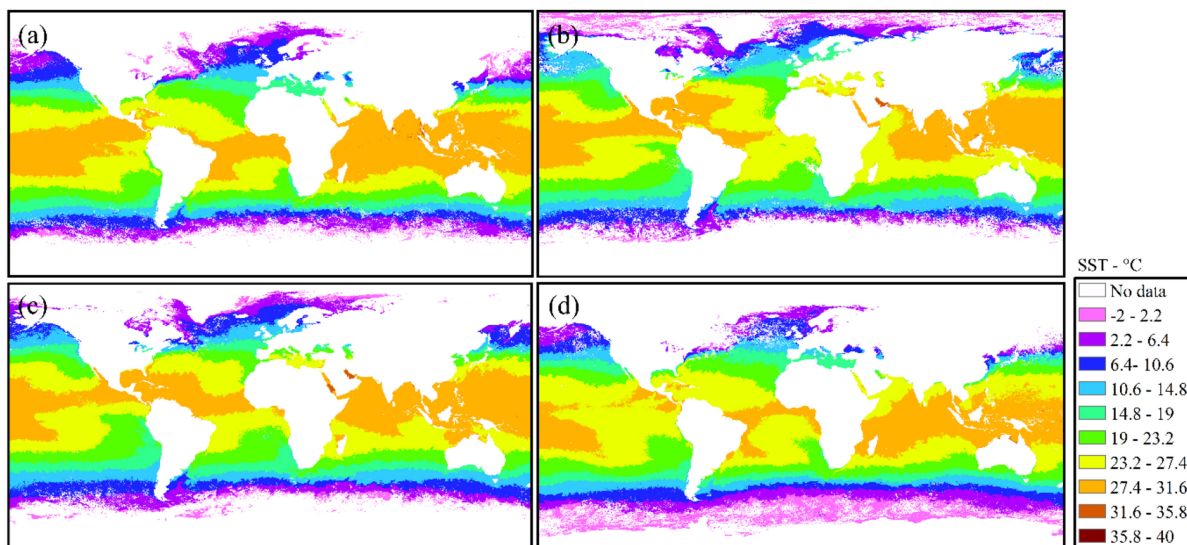
Fig. 3. Mean value of the global SST, generated using MODIS data in (a) January, (b) April, (c) July, and (d) October. No data values (white color) are related to land and clouds.

SST has been employed in many global, regional, and local studies. Monitoring ocean currents and El-Nino cycles [100]–[102], assessing the suitability of aquaculture ecosystem [103], [104], evaluating the thermal stress threat to coral bleaching [97], [105], understanding of climate warming [106]–[108], determining air-sea fluxes and CO_2 exchanges [109]–[112], monitoring diurnal variation [113], [114], and quantifying the development of severe storms [115], [116] are some of the primary applications of SST. For instance, Ferster et al. [101] analyzed 35-year SST observations to investigate the relation of SST anomalies with the Antarctic oscillation and the southern oscillation.

The SST observations from AVHRR were used to calculate the SST anomalies. The results showed a significant correlation between SST and both the AO and SO, indicating the warming and cooling effects in Southern Hemisphere and Antarctic regions, respectively.

In another study, the MODIS SST data acquired from 2015 to 2016 were employed to evaluate the relative importance of thermal stress on the coral bleaching phenomenon [97]. The SST anomalies were compared to in-situ measurements of coral bleaching that were identified through photo quadrats at four Islands in western Indonesia. A polynomial model was utilized as a statistical regression to model the relationship between SST and coral bleaching. The significant coefficient of determination proved that the SST anomalies were highly correlated with coral bleaching, indicating the potential of MODIS SST data for coral monitoring.

Furthermore, Wu *et al.* [103] developed an operational procedure to monitor the possible threat of cold-water disaster on Cobia fishes in the Penghu Islands region of Taiwan. They attempted to select suitable sites of the inner bay of the Penghu Islands to reduce losses and mortality rate of aquaculture fisheries. In this regard, AVHRR SST data, Chl, distance from coastal line, and cold-water intrusion day were utilized. These variables were classified into six categories based on biological characteristics and the environmental requirements of the Cobia fishes. Finally, the arithmetic and geometric mean were applied to evaluate the suitability of aquaculture sites.

IV. MICROWAVE RADIOMETERS

Microwave radiometers can be categorized into two groups of nonpolarimetric and polarimetric. These systems and their corresponding applications are discussed in the following two sections.

A. Nonpolarimetric Microwave Radiometers

Microwave radiometers are passive instruments and measure the electromagnetic radiation emitted from targets. Microwave radiation from the ocean mainly depends on its physical characteristics, such as surface roughness, SST, and OSS. Moreover, the propagation of microwave electromagnetic radiation through a material is determined by its electric conductivity, magnetic permeability, and electric permittivity. While electromagnetic waves propagate in dielectrics, they are reflected from conductive materials [113], [114].

Like other microwave RS systems, microwave radiometry is almost independent of sunlight, day/night, and weather conditions. Therefore, the radiations from oceans are constantly emitted, pass through clouds, and are not absorbed by the atmosphere. However, the atmosphere itself also emits microwave radiation that contaminates the radiation received by a microwave radiometer from oceans. Several approaches, called atmospheric sounding, have been developed to calculate and eliminate the radiation generated by the atmosphere [117], [118]. One of the common approaches for atmospheric sounding is to use channels of the microwave radiometer, which are primarily affected by atmospheric temperature and humidity radiations rather than other radiations emitted from the surface and to compute the emission of the atmosphere [119]. Moreover, although the radiations from oceans emit even when it is rainy, rain produces significant variations in the atmospheric BT. These variations decrease the accuracy of estimating different measurements, such as sea surface wave spectrum and wind speed [120].

1) Systems: Numerous microwave radiometers have been used for various RS applications over oceans. Table VI (see Appendix) provides the most commonly used microwave radiometers for ocean applications, the details of some of which are provided below.

The Electrically Scanning Microwave Radiometer (ESMR) was carried by Nimbus-5 at the height of 1100 km and was mapping the whole earth and its atmosphere continuously at various angles. Its main mission was measuring the liquid water content of clouds over oceans, soil moisture, surface decomposition, and SI on polar areas. A computer on board controlled the scanning process, which was symmetrically distributed in 78 independent scan spots extending 50° to either side of nadir. The spatial resolution of ESMR data was 25×25 km near nadir, but it was decreasing to 160-km cross-track by 45-km along-track at the ends of the scan [121].

The Scanning Multi-channel Microwave Radiometer (SMMR) was launched by Nimbus-7 in 1978 and worked until 1987 with a global coverage. It worked in five frequencies, 10 channels of the orthogonally polarized antenna temperature data with a spatial resolution of 25 km $\times$ 25 km [122], [123].

The Special Sensor Microwave/Imager (SSM/I) had seven orthogonally polarized channels in four frequencies, dual-polarized in all frequencies except the 22 GHz with only the vertical polarization. The next generation of the SMMR was carried by the Defense Meteorological Satellite Program (DMSP) satellites. The DMSP satellites have been orbiting in a near-circular, sun-synchronous, polar orbit with an altitude of approximately 850 km [123], [124]. SSM/I is a conical scanning radiometer with an incidence angle of 53.1° [117]. Observations of this sensor have been used for atmospheric, ocean, and terrain measurements [123].

The Special Sensor Microwave Imager/Sounder (SSMIS) is a passive microwave radiometer with 24 channels. The sensors' frequencies range from 19 to 183 GHz. SSMIS is a conical scanning radiometer with an incidence angle of 53.1° [123]. Among its primary mission, goals are meteorological, oceanographic, and solar-geophysical applications.

The Tropical Rainfall Measuring Mission (TRMM) was a research satellite that carried several sensors to provide information of precipitation, cloud liquid water, and water vapor within 35° north and 35° south of the equator at the height of 400 km. One of its sensors was the TRMM Microwave Imager (TMI). TMI, designed based on the SSM/I, was a multichannel passive microwave radiometer operating at five frequencies, dual-polarized, except for the 22 GHz, which was only at vertical polarization.

The Microwave Imaging Radiometer using Aperture Synthesis (MIRAS) is a microwave radiometer carried by the Soil Moisture and Ocean Salinity (SMOS) satellite. SMOS is a water mission launched by the ESA in 2009 and provides global observations at *L*-band, a frequency of 1.4 GHz, at a latitude of 758 km. SMOS is the first satellite to monitor the Earth's water cycle by observing OSS, soil moisture, snow, and SI [125]. By MIRAS measurements, it is possible to do polarimetric interferometric radiometry, which is one of the techniques to calculate OSS more accurately [126].

The measurements of the nonpolarimetric microwave radiometers have been applied to monitor SST, ocean surface wind (OSW) speeds, atmospheric water vapor, cloud liquid water, sea ice, and rain rate [118]. These applications are discussed further in the following section.

2) Applications: Radiometers' measurements are utilized to estimate different parameters, such as atmospheric water vapor, SST, cloud liquid water, rain rate, OSS, SI, and OSW. Since the focus of this study is ocean applications of various
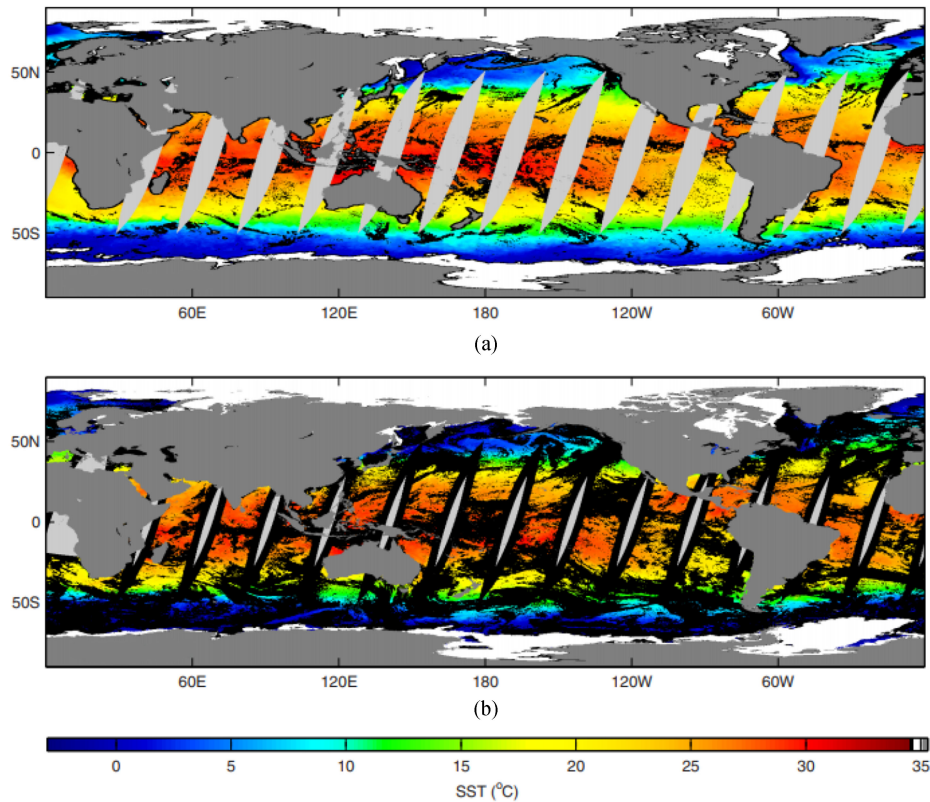
Fig. 4.   (a) AMSR-E and (b) MODIS SST maps produced for January 1, 2003 [137]. Light gray areas are where no data are collected between successive orbits (swath gaps) and black areas show missing data.

RS systems, those related to maritime surveillance are only discussed.

a) OSW Speed: The most crucial application of microwave radiometers is OSW speed estimation. Although it is relatively easy to estimate OSW speed using nonpolarimetric radiometric measurements, OSW direction estimation is ambiguous. The reason for this ambiguity is that the dependencies of both vertical and horizontal polarizations on the OSW direction are similar. Some other sources of information, such as weather prediction models or scatterometer measurements, are required to solve this ambiguity. A few research studies have been conducted to estimate the OSW direction from multiple parameters extracted from microwave radiometer measurements [127], [128].

Over ocean areas, the BT measured by microwave radiometers depends on the sea surface reflectivity. The sea surface reflectivity is a sum of gravity-generated specular reflectivity and wind-generated rough reflectivity. If the surface refraction index is known, it is possible to calculate the specular reflectivity for a specific wavelength and incidence angle using the Fresnel equation. Then, theoretically, the remaining part of the sea surface reflectivity is a function of the capillary sea waves generated by wind [129].

Many research studies have been so far conducted on OSW estimation from microwave radiometer data. For example, [129] used three different channels of AMSR-E to estimate OSW speed. They also used the tropical atmosphere-ocean data

as a reference. Their results showed the Root Mean Square Errors (RMSEs) of 00.37 m/s, 0.42 m/s, and 0.49 m/s for three frequencies of 18.7 GHz, 23.8 GHz, and E 36.5 GHz, respectively.

b) Sea Surface Temperature (SST): Although *in-situ* SST measurements are the average values of the SST over a specific period (e.g., every hour), the microwave radiometer data are instantaneous measurements averaged over large areas. The difference between these two measurements becomes more significant in regions near coastal lines where SST values have higher fluctuations based on time and location variations [130], [131]. Another difference between SST measurements from radiometers and *in-situ* buoys is related to the depth of the measurements. Microwave radiometers can measure SST at a few millimeters deeper than the water surface. However, buoy measurements are generally collected at 1.5–2 m depth [132]–[134]. The upper ocean is usually well mixed, and there is not much difference between measurements collected at 1-mm and 1-m depths, except during sunny days when there is low wind, and the water surface is warmer [135].

Microwave radiometers can measure SST with a relatively low spatial resolution (e.g., 25 km) in all weather conditions, except during severe rains, when the noise level is too high for reliable measurements. For instance, Fig. 4 presents a comparison of the MODIS and AMSR-E SST products. AMSR-E missing data are primarily due to rain; however, other missing

data are also evident near land and in the Northern Atlantic and Mediterranean regions with the huge amounts of manufactured structures due to radio frequency interference [136], [137]. MODIS has thinner swath gaps than AMSR-E but includes lower quality data at high incidence angles, which leads to missing data at the scan edges. Most other missing data in the SST map generated from MODIS data are caused by cloud presence [137].

Regarding the studies conducted on SST estimation from microwave radiometers, O'carroll *et al.* [138] showed the standard deviations of the SST measurements from the Advanced Along-Track Scanning Radiometer (AATSR), buoy, and AMSR-E were 0.14°C, 0.24°C, and 0.42°C, respectively. Additionally, Gentemann [137] performed a comparison between SST measurements from AMSR-E, MODIS, and buoys. They found that it was of great importance that a water vapor parameter was considered and eliminated from the AMSR-E measurements. However, they showed that AMSR-E measurements were more reliable than those of MODIS over cloudy areas and in high latitudes where the cold surface made a considerable bias in infrared measurements.

c) Ocean Surface Salinity (OSS): Emissivity is a dielectric property of an object and is an index showing the amount of its conductivity and radiation emission [139]. The emissivity of ocean water surface mainly depends on the amount of salt that water contains. Thus, microwave radiometer measurements can estimate OSS [126]. For instance, SMOS measures OSS at a depth of 1 cm [140]. Ocean salinity can be easily observed in microwave *P*-band channels with frequencies of 0.6–0.7 GHz. However, microwave *L*-band systems with frequencies of about 1.4 GHz are preferable for this purpose due to the relatively low spatial resolution and high galactic noise in the *P*-band channels. It is worth noting that the *L*-band data are also highly dependent on SST, radiometer incidence angle, and polarization [141]. One of the common approaches to decreasing the geometrical contributions in the estimation of OSS is polarimetric interferometric radiometry, which requires two simultaneous measurements from each location on the ocean to be considered. For example, MIRAS carried by SMOS is the sensor that makes it possible to implement such a technique [142]–[144]. Many studies retrieved OSS from SMOS products [145], [146]–[148]. For example, Pi-MEP [149] performed a systematic comparison between SMOS OSS products and those collected by the *in-situ* analysis system. It was observed that OSS calculation was less precise in areas near land due to the radiation contamination. The OSS root-mean-square difference in areas with distances of more than 800 km, between 150 to 800 km, and less than 150 km from coasts were approximately 0.19 pss, 0.32 pss, and 0.58 pss, respectively [150].

d) Sea Ice (SI): SI thickness is another marine application of microwave radiometers. SIs are typically classified into three classes of the first-year ice, multiyear ice, and ambiguous ice [151]. Ambiguous ice happens where thick snow on first-year ice might be confused with multiyear ice type and vice versa. The other issue with estimating SI is the lack of enough *in-situ* reference datasets for performing more accurate comparisons and evaluations of the satellite measurements [151].

B. Polarimetric Microwave Radiometer

Polarimetric microwave radiometers play an essential role in atmospheric, oceanic, and glaciology sciences. These types of sensors provide long-term observations of geophysical parameters (e.g., SST and dielectric constant) and surface geometric features (e.g., ocean surface roughness) using low microwave frequency data.

As discussed, nonpolarimetric radiometers cannot obtain the OSW direction due to the lack of information in cross polarization [127], [152]. In fact, the OSW direction can be retrieved using a combination of horizontal and vertical polarizations (first/second Stokes components) with the cross correlation of them (third/fourth Stokes components) [127], [152]. Therefore, determining the OSW direction requires full polarimetric information, which can be characterized by the modified Stokes vector [153]

$$I_s = \begin{bmatrix} I \\ Q \\ U \\ V \end{bmatrix} = \begin{bmatrix} T_v \\ T_h \\ T_{45} - T_{-45} \\ T_{\mathrm{lc}} - T_{\mathrm{rc}} \end{bmatrix} = \begin{bmatrix} \langle E_v E_v^* \rangle \\ \langle E_h E_h^* \rangle \\ 2\mathrm{Re} \langle E_v E_h^* \rangle \\ 2\mathrm{Im} \langle E_v E_h^* \rangle \end{bmatrix} \quad (4)$$

where T_v, T_h, T_{45}, T_{-45}, T_{lc}, and T_{rc} denote BTs at vertical, horizontal, $+45°$ and $-45°$ left-hand circular, and right-hand circular polarizations, respectively [127].

1) Systems: WindSat is the only spaceborne multifrequency polarimetric microwave radiometer that is capable of measuring OSW vectors (i.e., both OSW speed and direction) [152]. This sensor was designed at the US Naval Research Laboratory (NRL) through sponsor-funded by US Navy and the National Polar-orbiting Operational Environmental Satellite System (NPOESS) Integrated Program Office (IPO) [152]. It was deployed on the Coriolis spacecraft, which was successfully launched from Vandenberg Air Force Base (VAFB), California, into a sun-synchronous orbit (830-km; 98.7° orbit) on January 6, 2003 [150]. Although WindSat was developed with a 3-year mission design life, it is still active. With both positive and negative maneuvers of scanning beams, BT is measured over azimuth positions of 0° (looking forward) and 180° (looking aft) approximately of 1400 km and 750 km, respectively [152], [153]. Although WindSat is conically scanning, the data acquisition is limited at specific scan angles due to inadequate calibration tools [154], [155]. Moreover, the calibration configuration is restricted in the aft swath range for the WindSat geometry and various angles [152]. However, enough data are provided in dual-look versus the single-look in retrieving the OSW vector by WindSat [152], [155].

WindSat contains 22 microwave channels operating at five different frequencies: 6.8, 10.7, 18.7, 23.8, and 37 GHz [156]. The 10.7-, 18.7-, and 37.0-GHz channels have the full polarimetric capability and are specially used to measure OSW vector based on four modified Stokes radiometric parameters [127], [156]. The 6.8- and 23.8-GHz channels are dual-polarized and are mostly employed to measure SST and water vapor, respectively [152].

2) Applications: WindSat showed the capability of using a fully polarimetric radiometer to accomplish following three main objectives [155]:

1) reconstructing and measuring the OSW speed and direction (primary measurements);
2) retrieving the additional environmental parameters, such as SST, soil moisture, SI and snow, integrated atmospheric water vapor, cloud liquid water, and rain rate (secondary measurements);
3) providing reliable polarimetric radiometer data to use in developing the NPOESS Conical Microwave Imagery and Sounder (CMIS).

WindSat products are mainly provided by the RS Systems (RSS) [157] by supports from the NASA Earth Science MEaSUREs DISCOVER Project and the NASA Earth Science Physical Oceanography Program [158], [159]. The RSS WindSat data are produced in daily and time-averaged products (3-day, weekly, and monthly) in the binary data files [158], [159]. Despite the daily products, which have the UTC observation time, the time-averaged products do not have any time information [158]. The daily and 3-day products are generally affected by gap data where such a problem is less in the weekly and monthly products due to the averaging of observations. Each daily, 3-day, weekly, and monthly product is gridded at $0.25° \times 0.25°$ on ascending and descending passes. Fig. 5 illustrates WindSat products generated by RSS.

WindSat data have been widely used in different applications. For example, Zhang *et al.* [160] developed a novel model for retrieving hurricane OSW speed using the 6.8 GHz and 10.7 GHz vertical/horizontal polarized BTS. This model was developed and validated using WindSat observations over 15 hurricanes between 2003 and 2010. Their method had reasonable results in estimating hurricane OSW speeds over the ocean surface. Moreover, good agreement was found between the retrieved OSW speeds from this satellite with the ones generated from the Stepped-Frequency Microwave Radiometer (SFMR). Moreover, Zheng *et al.* [161] presented an inclusive comparison of the OSW vector measured by HY-2A scatterometer (*Ku*-band scatterometer) and WindSat between October 2011 and September 2015 in the global oceans. The statistical results showed no significant difference between the HY-2A scatterometer and WindSat OSW speed products, where the difference was considerable in the OSW direction. Moreover, a significant difference was observed in the westerlies in both hemispheres.

V. GNSS-Reflectometry (GNSS-R)

The Global Positioning System (GPS) was developed more than 30 years ago, originally for positioning, navigation, and timing purposes. The GPS and other GNSS signals pass through the atmosphere or reflect from different Earth's surfaces (e.g., land, ice, and ocean) and contain valuable information from different geophysical parameters. Currently, these signals are used not only for navigational purposes but also for diverse RS applications.

The exploitation of the reflected GNSS signals from the Earth's surface is an RS technique known as GNSS Reflectometry (GNSS-R, Fig. 6). A large variety of geophysical properties can be retrieved from the measurements of GNSS-R receivers on different ground-based, airborne, and spaceborne platforms (see [162] for more details). In this study, we limit our review to the RS of the ocean using spaceborne GNSS-R measurements. Here, we classify GNSS-R systems as those operating in passive configuration since they normally carry no active instruments but note that the signals are still emitted actively onboard other independent (i.e., GNSS) satellites.

The exploitation of GNSS signals reflected from the ocean surface as a multistatic scatterometry concept was initially discussed in 1988 [164]. In the late 1990s, the feasibility of using GNSS-R observations to retrieve ocean surface roughness and OSW speed was demonstrated in airborne experiments [165], [166]. In 1993, the application of GNSS-R systems to determine ocean surface height (OSH) was also proposed in the concepts of the Passive Reflectometry and Interferometry Systems (PARIS) [163].

The theoretical ideas were followed by evidence on the technical feasibility of implementing the technique in spaceborne missions. In 1994, the reflected signals of the GPS were received onboard the Spaceborne Imaging Radar-C (SIR-C), which was a piece of evidence that the reflected signals are trackable from space [167]. The signature of the GPS signals in the radio occultation measurements of GPS/Meteorology and Challenging Minisatellite Payload (CHAMP) provided further insights into the signal-to-noise ratio (SNR) of the reflections [168], [169]. These events motivated the launch of the spaceborne GNSS-R missions.

The technique observations of GNSS-R generally rely on the cross correlation of the reflected signal, received at a down- or side-looking antenna, with a locally generated replica of the transmitted signal-conventional GNSS-R—or with the direct signal itself usually received at the up-looking antenna-interferometric GNSS-R (iGNSS-R).

The cross-correlation power is normally recorded for a set of different time lags, compensating the signal delay, and different carrier frequency offsets, due to the Doppler shifts caused by relative movement of the receiver and transmitter, which outputs the delay-Doppler Maps (DDMs). If the frequency offset is considered fixed, the receiver can be limited to generating a 1-D map of power at that specific frequency known as a waveform. In other words, a waveform is a cut of a DDM at the fixed frequency shift. Theoretical models describe the correlation power as a function of technical properties, reflection geometry, and the surface state, among which the bistatic radar equation proposed in 2000 is well known [170]. The correlation power in the DDMs is proportional to the bistatic radar cross section σ^0 being, in turn, a function of ocean surface roughness and, consequently, OSW speed. It can be theoretically derived from upwind and crosswind ocean slope components obtained from surface models, such as those proposed in [171] and [172]. Fig. 7 shows σ^0 derived from ocean state simulated using Cox and Munk's [172] surface model. Fig. 8 also visualizes the DMMs obtained at different wind speeds.
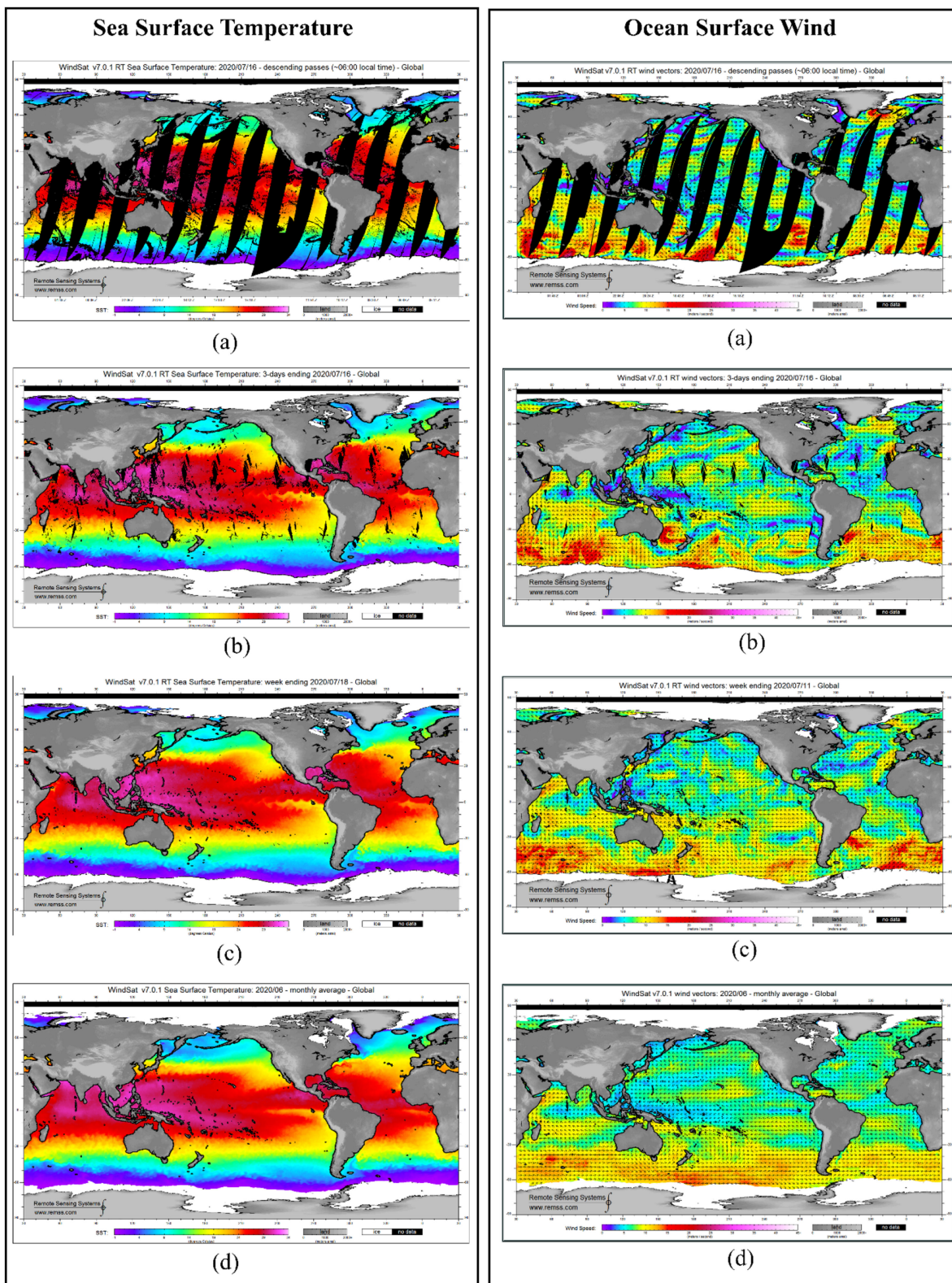
Fig. 5.   WindSat SST and OSW products generated by the RSS. (a) Daily product in 2020/07/16. (b) Average of 3 days ending: 2020/07/16. (c) Average of the week ending: 2020/07/11. (d) Average of month: 2020/06.
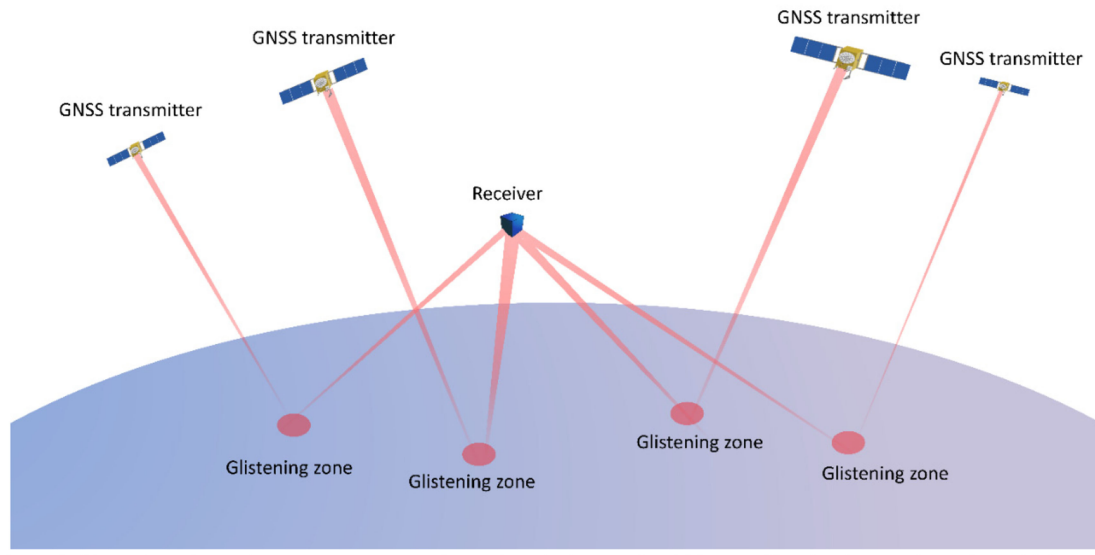
Fig. 6.   Schematic illustration of spaceborne GNSS-R: A receiver onboard a low Earth-orbiting satellite simultaneously tracks multiple reflected GNSS signals.
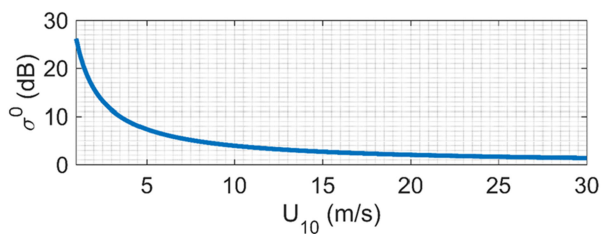

Fig. 7.   Simulated bistatic radar cross section σ^0 as a function of ocean wind speed at 10 m above the surface U_{10}.

The signal power in the DMMs is inversely proportional to OSW speed. Different observables can be extracted from the DDMs representing the dependence to OSW speed (or other target geophysical parameters). Finally, these observations are mapped to OSW speed through a mapping function, which is determined based on theoretical knowledge or in an empirical sense [173], [174].

Suppose the signals are scattered from rough enough surfaces (e.g., at high winds—theoretically larger than 4–5 m/s). In that case, most of the signal energy is scattered in different directions and, thus, incoherent reflection or strong diffuse scattering happens. When the ocean is calm, or the signal is reflected by an ice surface, a coherent reflection appears. As a result, the total power is considered to summarize the coherent and incoherent components when such a weak diffuse scattering happens. Accordingly, the bistatic radar equation was revisited and proposed in 2018 [175]. Additionally, a model was proposed describing such a weak diffuse scattering providing a smooth transition to strong diffuse scattering regimes [175]. Fig. 9 compares the DMMs for weak and strong diffuse scatterings. The left DDM represents the power of the signal reflected from a first-year ice surface. In this DDM, a combination of incoherent and coherent scattering is evident. The coherent component has appeared as

a strong single-point power with a horizontal extension over the Doppler frequency shift. The coherent component is shown along with a weak incoherent component that appeared in a horseshoe shape. The right DDM shows no coherent component representing the power of the signal reflected from a rough enough ocean surface.

A. Systems

Table VII (see Appendix) summarizes the launched or planned GNSS Reflectometry mission or those with accomplished Phase-A studies developed—or potentially can be used—to study oceans. More details of some of these missions are discussed ahead.

The bistatic forward scatterometry technique using GNSS signals motivated the launch of the first demonstration satellite missions, the U.K. Disaster Monitoring Constellation (U.K.-DMC), in 2003 [176]. The U.K.-DMC was launched into a 680-km sun-synchronous orbit in 2003 and carried the first spaceborne receiver dedicated to GNSS-R. The receiver cross correlated the reflected signal from a nadir-looking antenna with a signal replica producing the DDMs.

With the lessons learned from U.K.-DMC, the TechDemoSat-1 (TDS-1) satellite mission was designed and launched into a 635-km Low Earth Orbit (LEO) on July 8, 2014 [177], [178]. TDS-1 carried the autonomous Space GPS Receiver Remote Sensing Instrument (SGR-ReSI). The SGR-ReSI tracked the GPS L1 Coarse/Acquisition code reflections and the L2 signals for the first time. TDS-1 was a shared space platform with other experiments and provided DDMs every two days out of fourteen. The extensive investigations on the TDS-1 datasets, which were substantially larger than those of the U.K.-DMC, further broadened the knowledge on spaceborne GNSS-R and its potentials. Acceptable OSW speeds were obtained from the DDMs [179], [180]. The TDS-1 also shows the suitability of the technique in
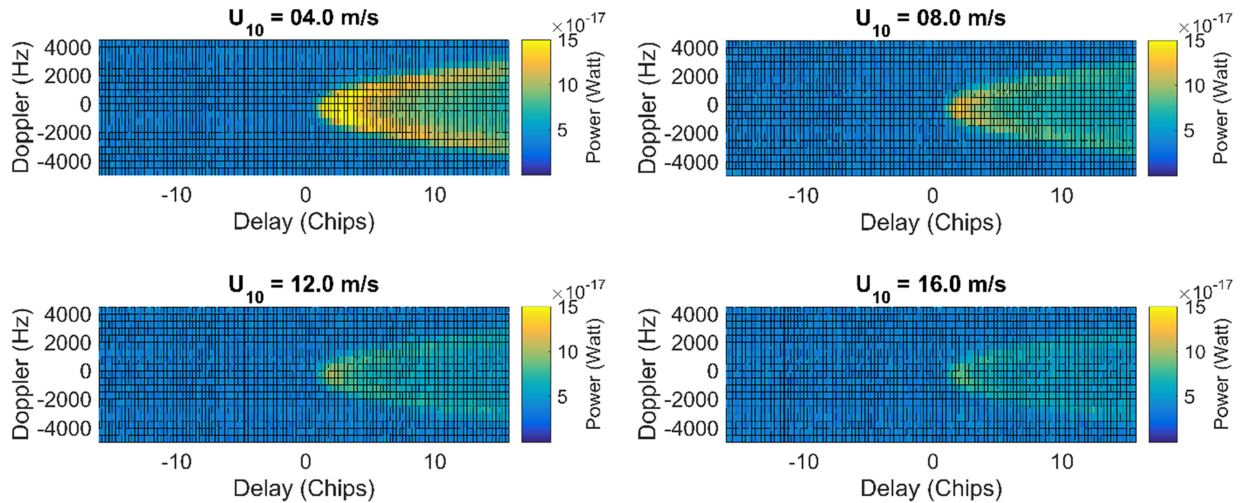
Fig. 8. Simulated DDMs recorded by a receiver tracking GPS signals onboard a satellite orbiting at the altitude of 825 km, at an incidence angle of 30° and different wind speeds U_{10}.
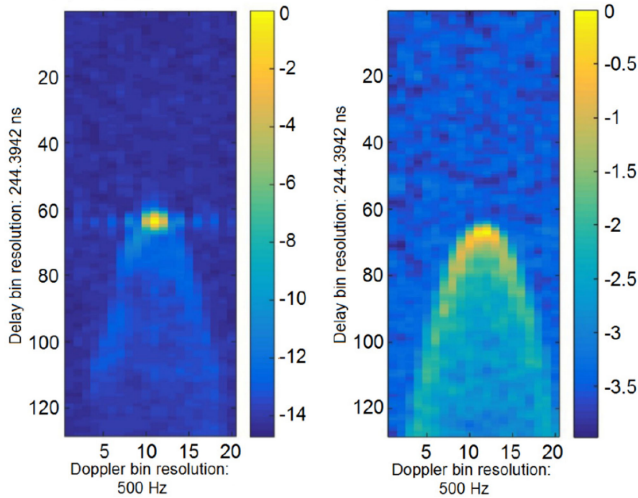

Fig. 9. DDMs recorded tracking signals reflected from a first-year ice (left) and a rough ocean surface (right) [175], [196].

data collection in severe weather conditions. It was observed that the OSW speed estimations had a higher level of stability during rainfall in comparison to conventional scatterometers [179], and the signals were trackable in severe weather conditions [181]. TDS-1 was a significant experiment enhancing the maturity of the technique. It tracked reflected signals until December 16, 2018, when the GNSS-R data collection ceased, approaching its end of life in May 2019.

Recognizing the potentials of the GNSS-R technique, NASA developed the first constellation of satellites, fully dedicated to GNSS-R. The Cyclone Global Navigation Satellite System (CYGNSS) was launched on December 15, 2016. It comprises eight micro-satellites in 35° inclined orbits. The main objective of this mission was estimating OSW, specifically in the inner core of tropical cyclones. The derived knowledge

and products are improving the forecasting and tracking of hurricanes [182].

The low mass and power consumption of GNSS-R sensors ease the implementation onboard small and inexpensive satellites. The receivers simultaneously track multiple GNSS transmitters signals, which are reflected from distinct areas, offering an unprecedented sampling rate with high spatial coverage. Moreover, *L*-band GNSS signals are insignificantly attenuated passing through a rainy atmosphere, leading to the robustness of the OSW speed retrievals in such conditions [183]. These advantageous characteristics motivate scientists for novel ideas on future missions. For example, a team of 17 scientists in different European countries assessed GNSS-R, Radio Occultation, and Scatterometry onboard the International Space Station (GEROS-ISS) [184]. The idea was proposed to the ESA in 2011. A GNSS-receiver at the upper external payload facility (upper balcony) of the Columbus module was considered. The primary motivation of GNSS-R onboard the ISS is ocean altimetry and RS of the surface state. The GNSS Transpolar Earth Reflectometry exploriNg system (G-TERN) is the other GNSS-R mission proposed and studied as a response to the ESAs Earth Explorer revised call [185]. The scientific objective of G-TERN is the RS of SI properties. Furthermore, the mission was proposed for monitoring other ocean system components, such as OSW.

B. Applications

Numerous studies have been conducted using ground-based and airborne GNSS-R experiments on different applications, scaling up the technique to space missions. We note again that this review focuses only on spaceborne studies for ocean application; however, promising results are also achieved using GNSS-R measurements over land (e.g., [168], [169], [170]). It is also worth noting that the GNSS-R is still a young RS technique whose potentials are still being explored. We introduce here the
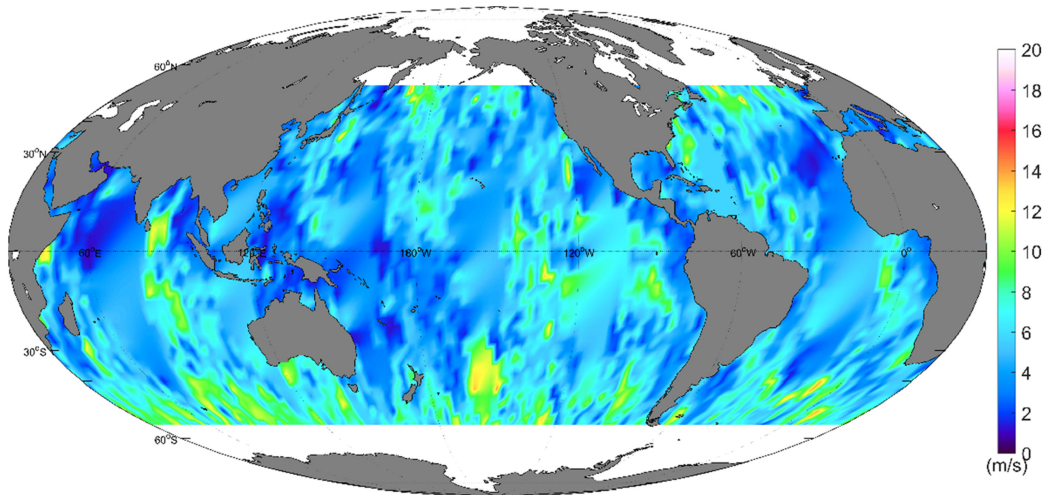
Fig. 10. Average global wind speed obtained from TDS-1 measurements from May 2015 to June 2016 [179].

currently typical ocean applications, as well as some of the future possibilities.

1) OSW Speed: Monitoring OSW speed is a well-established application of spaceborne GNSS-R. The first evidence on the capabilities of spaceborne GNSS-R in obtaining OSW speed was shown in 2005 when the data analysis of U.K.-DMC measurements demonstrated the promising trends between OSW and waves and DDMs [176]. The obtained spaceborne GNSS-R OSW speed data resulted in the RMSE of 1.84 m/s compared to buoy observations at low to moderate winds [186]. Additionally, the TDS-1 measurements led to acceptable OSW products in 2015 [180]. A new dataset was developed using the same data and was validated using the data acquired by conventional scatterometers [179]. Fig. 10 visualizes the average global OSW speed derived from TDS-1. The evaluations demonstrated the robustness of the OSW products during rainfall, being a piece of evidence on the suitability of the technique for monitoring OSW in extreme weather. The effect of rain atmospheric signal attenuation on the OSW speed products was ignorable [183].

The CYGNSS, being fully dedicated to GNSS-R and with the lessons learned from TDS-1, is also able to provide higher quality OSW speed data. Overall RMSE of the CYGNSS OSW wind retrievals is 1.4 m/s at speeds lower than 20 m/s [187]. However, it should be noted that the OSW products are subjected to improvement as the physical understanding and retrieval algorithms are being enhanced. The CYGNSS has further demonstrated the capability of the technique to track hurricanes with high sampling rates and improve weather forecasts. For example, Fig. 11 shows CYGNSS observations from hurricane Harvey [182]. It is also shown that the assimilation of CYGNSS data into weather models will improve tracking hurricanes, forecasting their intensity, and structure especially for the weak phase of a hurricane [188], which has been one of the main motivations for developing CYGNSS.

The retrieval algorithms for OSW speed estimation for GNSS-R data are generally an inversion of an observable to OSW information. The observable is a quantity extracted or computed
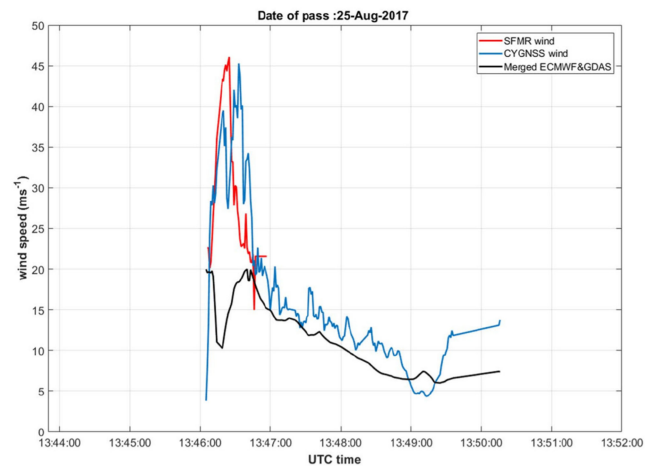

Fig. 11. CYGNSS measurements of surface wind speed from Hurricane Harvey in blue along with coincident measurements by the Stepped Frequency Microwave Radiometer (SFMR) instrument on the P-3 in red and the ECMWF predicted wind speed in black [182].

from the measured waveforms or DDMs, which is necessarily sensitive to the ocean state and OSW speed. In [174], the authors developed an algorithm to determine OSW speed based on a scattering model generating sets of waveforms. They used the bistatic radar equation to predict the shape of the cross-correlation waveform at different OSW speeds. The measured delay waveforms can be fitted in a least-squares sense to those derived from theoretical models. In [189], the authors have proposed a method to obtain both OSW speed and direction by matching simulated GNSS-R DDMs to the measured one. Currently, there is a variety of approaches implemented for ocean OSW estimation using GNSS-R data. Recently, traditional machine learning techniques have also shown promising results [190]–[192]. However, the deep learning techniques have not yet been well investigated due to the novelty of the GNSS-R techniques. It is expected that deep learning can play a crucial role in utilizing GNSS-R data more efficiently, mainly due to the
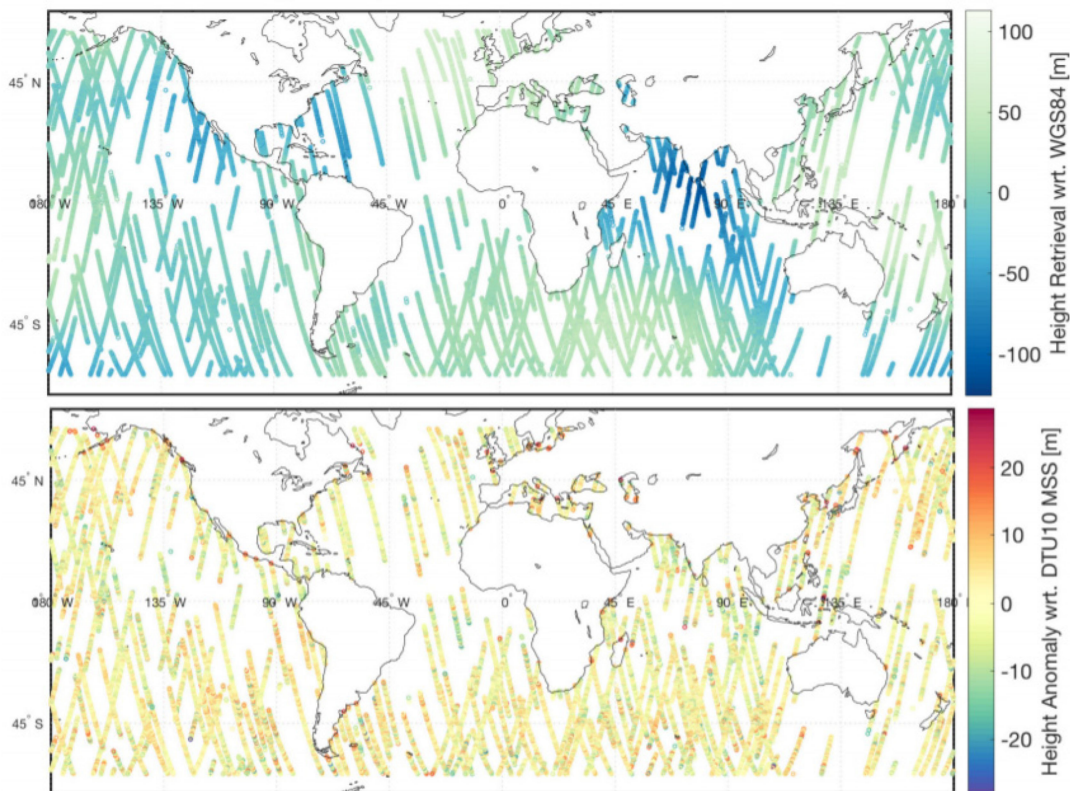
Fig. 12.   Ocean surface topography derived from TDS-1 measurements with respect to the WGS84 reference ellipsoid (up) and the anomaly with respect to DTU10 mean sea surface (bottom) [203].

substantially larger GNSS-R datasets compared to conventional instruments.

2) Sea Ice (SI): In 2003, RS of SI using spaceborne GNSS-R was discussed by proposing a model to describe the ice scattering mechanism [193]. In 2006, it was argued that there was a strong presence of the coherent component in GNSS-R SI bistatic signal scattering [194]. This was further investigated using TDS-1 measurements in 2010, characterizing its feasibility for SI studies [195]. Later, the GNSS-R reflected signals recorded by TDS-1 were used for SI detection in [196]. They proposed a probabilistic Bayesian model and reported an SI detection probability of 98.5%, a false alarm probability of $\sim 3.6\%$, and an error probability of 2.5%, as the best results. Using machine learning techniques, more specifically by exploiting support vector machine algorithms, an improvement in SI detection was reported in [197]. An effective schematic was recently proposed for obtaining SI thickness using TDS-1 measurements, and good agreement between the TDS-1 results and the reference data was reported [198]. Differential delay waveform was also proposed as a new observable to estimate SI concentration [199]. Furthermore, promising results were achieved to classify ice types during the SI formation using TDS-1 measurements. The derived information was compared to synthetic aperture radar (SAR)-derived SI-type maps [199]. The comparison evaluated the derived classifications of SI-open water samples with a success rate of 97%, and SI-type classification of first-year, multiyear, and young ice with satisfactory accuracies of 70%, 82%, and 81%, respectively.

3) Altimetry: The exploitation of GNSS signals for ocean altimetry was first proposed in 1993 [163]. Similar to conventional radar altimeters, GNSS-R receivers can track the time delay of the reflected signal and, consequently, can estimate Ocean Wave Heigh (OWH) with respect to the position of the receiver. The code and carrier phase observations can be employed to obtain the path delay of the reflected signals regarding the direct signal; a tutorial is given in [163]. Using the carrier phase requires a calm ocean resulting in coherent enough reflections. This condition can be more easily met for altimetry over ice sheets. Altimetry using code delay observations estimates the delay through the cross correlation of the reflected signal with the replica or the direct signal. The low level of the reflected signal power and the limited bandwidth of GNSS signals impose limitations for code delay altimetry [200].

The capabilities of spaceborne GNSS-R in determining OSH were shown using TDS-1 measurements in [201]. The authors estimated OSH processing overpasses collected for six months. The capability of altimetry over ice sheets has been well demonstrated [202]. Later, global ocean altimetry was carried out using TDS-1 data, and the derived mean sea surface topography was evaluated in comparison to the WGS84 reference ellipsoid and DTU10 mean sea surface model from the Technical University of Denmark [203].

The comparison is visualized in Fig. 12. The authors described ionospheric delays and the receiver orbits uncertainty as the main limiting error budgets. They expected improved estimation accuracy in the future when better knowledge on
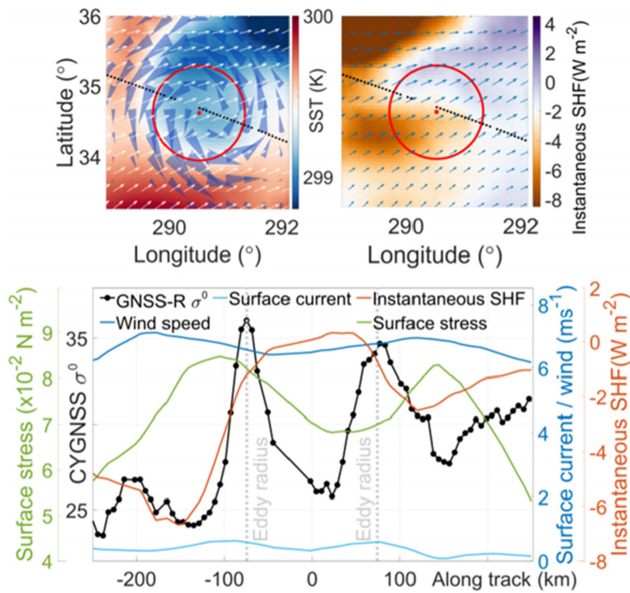
Fig. 13. CYGNSS observations are overpassing: SST, surface wind shown in white arrows, and currently shown blue cones (top-left). Instantaneous surface sensible heat flux along with surface stress is shown in blue arrows (top-right). The bottom panel shows the CYGNSS Bistatic Radar Cross Section $\sigma 0$ profile as well as the wind and current velocity, instantaneous sensible heat flux and surface stress magnitudes, referenced at the center of the middle eddy [206].

these errors is provided. Similarly, OSH was obtained using CYGNSS measurements with the two-way ranging precision reaching 3.9 m and 2.5 m [200]. TDS-1 and CYGNSS are optimized for scatterometry missions that require the orbit and the ionosphere delay information not as precise as those needed for ocean altimetry. Future GNSS-R missions dedicated to this objective could, therefore, lead to higher quality altimetry products.

4) Mesoscale Eddies: Based on high precision GNSS-R altimetric observations, RS of mesoscale eddies has been perused using airborne measurements [204], [205]. Due to the limitations discussed in Section V-B3, the characteristics of the spaceborne altimetric observations response over the mesoscale eddies have not yet been determined, despite the recent available large datasets acquired from GNSS-R satellite missions. In [206], the authors reported a distinguishable response of the GNSS-R scatterometric measurements over mesoscale ocean eddies. They discussed potential mechanisms causing the observed trend and considered the eddy-induced changes in the sensible heat flux and surface stress as the factors affecting the bistatic radar cross section σ^0. Fig. 13 shows an exemplary case σ^0 fluctuations over the eddy edges. Once the scatterometer records the information of the eddy-affected area, σ^0 jumps and then drops quickly at the center and then jumps once again as the track leaves the eddy. This preliminary study signified future investigations that could potentially lead to monitoring of mesoscale eddies using spaceborne GNSS-R measurements.

5) Ocean Precipitation: It is shown that the rain splash, i.e., the altered roughness by raindrops intruding the ocean surface, results in a reduction of the bistatic radar cross-section value [207]. Asgarimehr *et al.* [207] approved the existence of rain

signature in GNSS-R observations at low wind speeds (i.e., below 6 m/s), based on simulations and empirical analysis of TDS-1 data. It was concluded that GNSS-R could potentially detect rain over oceans at weak winds. The signature was later reported in CYGNSS measurements, with a similar explanation at low winds. It is recently shown that combining the measurements of reflected signals in different polarizations can potentially better help to track the precipitation modifications over oceans [208]. Conversion of the signature to rain information is still under investigation, trying to expand spaceborne GNSS-R applications to RS of ocean precipitation.

VI. CONCLUSION

RS systems offer great advantages for studying the physical, chemical, and biological features of the oceans. This study comprehensively discussed four main passive RS systems, which provide numerous opportunities for studying different oceanographic applications.

ORSS is based on the principal measurement of WLR and is widely used to study the ocean water constituents, such as Chl, CDOM, SPM, SI, OSS, particulate organic, and suspended sediments. The underlying concept is that the ocean water constituents influence water properties, such as color, scattering, attenuation, light-absorbing bands, BT, and dielectric constant, all of which are quantifiable using optical regions of the electromagnetic spectrum. MODIS, Sentinel-2, Sentinel-3, and Landsat-8 are the most commonly used ORSSs applied in ocean studies. ORSSs have synoptic coverage with various spatial and temporal resolutions. They can also provide long-term and consistent historical observations. These features, along with the possibility of near-real-time observations, make them appropriate systems for ocean studies. Nevertheless, the main limitation of these systems is that they can only operate during the daytime and cannot observe under clouds.

TIR radiometer is another passive RS instrument that uses the electromagnetic spectrum's thermal part to measure SST. To date, various methods from empirical models to the RT models have been developed to calculate SST values through the measured BTs. MODIS, ASTER, AHVRR, and ABI are the most commonly used TIR radiometers for various oceanographic applications.

Microwave radiometers measure the ocean surface's microwave radiation, which is directly influenced by physical characteristics of the ocean, such as surface roughness, SST, and OSS. Given the number of Stokes' parameters that these radiometers measure, microwave radiometers are categorized into two groups of nonpolarimetric and polarimetric systems. ESMR, SMMR, SSM/I, SSMIS, TRMM, SMOS, AMSR, and WindSat are some of the commonly used microwave radiometers for ocean studies. The observations of these satellites and missions can be applied to estimate various characteristics of the ocean, including OSW, SST, OSS, and SI.

The space-based GNSS-R system can detect and provide geophysical information about the ocean. The investigation, monitoring, and mapping of OSW speed, ocean roughness, SI conditions, ocean height, mesoscale eddies, and ocean precipitation are just some of many GNSS technique applications.

APPENDIX

TABLE VI
MICROWAVE RADIOMETERS FOR OCEAN STUDIES

Satellite	Sensor	Temporal resolution (days)	Spatial resolution (km)	Center Frequency (GHz)	Time period
Coriolis	WindSat	8	8 x 13 to 39 x 71	6.8-37	2003-ongoing
DMSP- F8 -F13	SSM/I	1	15 x 13 to 69 x 43	19.35-85.5	1987-2008
DMSP-F15-F19	SSMIS	1	15 x 13 to 69 x 43	19-91	2000-ongoing
GPM	GMI[6]	2	4 x 6 to 19 x 32	10.65-183.31	2014-ongoing
JAXA's ADEOS-II	AMSR	1	3.1 x 5.4 to 40 x 70	6.925-89	2002-2003
JAXA's GCOM-W1	AMSR-2	1	3 x 5 to 35 x 62	6.925-89	2012-ongoing
NASA's Earth Observing System (EOS) Aqua spacecraft	AMSR-E	1.5	6 x 4 to 75 x 43	6.9-89	2002-2011
Nimbus 5	ESMR	1	25 x 25	19	1972-1977
Nimbus-7	SMMR	2	22-120	6.6-37	1978-1987
OceanSat-1 (IRS-P4)	MSMR[3]	1	22 x 34 to 68 x 105	6.6-21	1999-2010
Priroda (Mir station)[**]	IKAR-N	-	60	13-89	-
Priroda (Mir station)[**]	IKAR-D	-	60	13-36.5	-
Priroda (Mir station)[**]	IKAR-P	-	8 x 12 to 25 x 33	13-36.5	-
Priroda (Mir station)[**]	R-400	6	-	7.5	-
SMOS	MIRAS	23	35-50	4-18.4	2009-ongoing
TRMM	TMI	1/2	5 x 7 to 37 x 63	10.7-85.5	1997-2015

TABLE VII
GNSS-R SYSTEMS FOR OCEAN STUDIES

Mission	Year of launch	Main application (not limited to)
UK-DMC [176]	2003	surface state and wind
TDS-1[178]	2014	surface state and wind
CYGNSS [182]	2016	ocean surface state and wind
[3]Cat-2[209]	2016	ocean altimetry
BuFeng-1 A/B [210]	2019	surface state and wind
Spire [211]	2019	surface state and wind, sea ice
Fengyun-3 series [212]	2020	surface state and wind
[3]Cat-5 A/B (FSSCat mission) [213]	2020	sea ice
PRETTY [214]	2021	altimetry
Formosat-7R [215]	2022	surface state and wind
PARIS-IoD [216]	Phase-A	altimetry
GEROS-ISS [184]	Phase-A	ocean altimetry, surface state and wind
G-TERN [185]	Phase-A	sea ice

REFERENCES

[1] R. Costanza, "The ecological, economic, and social importance of the oceans," *Ecological, Econ., Social Importance Oceans*, vol. 31, no. 2, pp. 199–213, Nov. 1999, doi: 10.1016/S0921-8009(99)00079-8.

[2] C. M. Lalli and T. R. Parsons, *Biological Oceanography: An Introduction*, 2nd ed. Oxford, U.K.: Butterworth-Heinemann, 1997.

[3] L. Cheng, J. Abraham, Z. Hausfather, and K. E. Trenberth, "How fast are the oceans warming?," *Science*, vol. 363, no. 6423, pp. 128–129, Jan. 2019, doi: 10.1126/science.aav7619.

[4] J. D. Santos, I. Vitorino, F. Reyes, F. Vicente, and O. M. Lage, "From ocean to medicine: Pharmaceutical applications of metabolites from marine bacteria," *Antibiotics*, vol. 9, no. 8, Jul. 2020, Art. no. 455, doi: 10.3390/antibiotics9080455.

[5] G. K. Devi, B. P. Ganasri, and G. S. Dwarakish, "Applications of remote sensing in satellite oceanography: A review," *Aquatic Procedia*, vol. 4, pp. 579–584, 2015, doi: 10.1016/j.aqpro.2015.02.075.

[6] H. Zhang, E. Devred, A. Fujiwara, Z. Qiu, and X. Liu, "Estimation of phytoplankton taxonomic groups in the Arctic Ocean using phytoplankton absorption properties: Implication for ocean-color remote sensing," *Opt. Exp.*, vol. 26, no. 24, pp. 32280–32301, 2018.

[7] M. J. Devlin *et al.*, "Combining in-situ water quality and remotely sensed data across spatial and temporal scales to measure variability in wet season chlorophyll-A: Great Barrier Reef Lagoon (Queensland, Australia)," *Ecological Processes*, vol. 2, no. 1, 2013, Art. no. 31, doi: 10.1186/2192-1709-2-31.

[8] IOCCG, *Earth Observations in Support of Global Water Quality Monitoring*. Dartmouth, NS, Canada: Int. Ocean Colour Coordinating Group, 2018.

[9] L.-L. Fu, T. Lee, W. T. Liu, and R. Kwok, "50 years of satellite remote sensing of the ocean," *Meteorological Monographs*, vol. 59, pp. 5.1–5.46, 2019, doi: 10.1175/AMSMONOGRAPHS-D-18-0010.1.

[10] R. J. W. Brewin *et al.*, "The ocean colour climate change initiative: III. A round-robin comparison on in-water bio-optical algorithms," *Remote Sens. Environ.*, vol. 162, pp. 271–294, 2015.

[11] H. Liu, Q. Zhou, Q. Li, S. Hu, T. Shi, and G. Wu, "Determining switching threshold for NIR-SWIR combined atmospheric correction algorithm of ocean color remote sensing," *ISPRS J. Photogrammetry Remote Sens.*, vol. 153, pp. 59–73, 2019.

[12] H. R. Gordon, "Some reflections on thirty five years of ocean color remote sensing," in *Oceanography From Space*. Dordrecht, The Netherlands: Springer-Verlag, 2010, pp. 289–306.

[13] T. Dickey, M. Lewis, and G. Chang, "Optical oceanography: Recent advances and future directions using global remote sensing and in situ observations," *Rev. Geophys.*, vol. 44, 2006, Art. no. 1.

[14] P. Dorji and P. Fearns, "Atmospheric correction of geostationary Himawari-8 satellite data for total suspended sediment mapping: A case study in the coastal waters of Western Australia," *ISPRS J. Photogrammetry Remote Sens.*, vol. 144, pp. 81–93, 2018.

[15] X. He, K. Stamnes, Y. Bai, W. Li, and D. Wang, "Effects of earth curvature on atmospheric correction for ocean color remote sensing," *Remote Sens. Environ.*, vol. 209, pp. 118–133, 2018.

[16] A. G. Myasoedov, V. N. Kudryavtsev, B. Chapron, and J. A. Johannessen, "Sunglitter imagery of the ocean surface phenomena," in *Proc. SeaSAR*, 2010, Art. no. ESA SP-679.

[17] V. Kudryavtsev, A. Myasoedov, B. Chapron, J. A. Johannessen, and F. Collard, "Joint sun-glitter and radar imagery of surface slicks," *Remote Sens. Environ.*, vol. 120, pp. 123–132, May 2012, doi: 10.1016/j.rse.2011.06.029.

[18] L. Feng *et al.*, "Exploring the potential of Rayleigh-corrected reflectance in coastal and inland water applications: A simple aerosol correction method and its merits," *ISPRS J. Photogrammetry Remote Sens.*, vol. 146, pp. 52–64, 2018.

[19] M. Wang and H. R. Gordon, "Sensor performance requirements for atmospheric correction of satellite ocean color remote sensing," *Opt. Exp.*, vol. 26, no. 6, Mar. 2018, Art. no. 7390, doi: 10.1364/OE.26.007390.

[20] X. He, D. Pan, Y. Bai, Z. Mao, and F. Gong, "General exact Rayleigh scattering look-up-table for ocean color remote sensing," *Remote Sens. Mar. Environ.*, vol. 6406, 2006, Art. no. 64061D.

[21] G. Liu, Y. Li, H. Lyu, S. Wang, C. Du, and C. Huang, "An improved land target-based atmospheric correction method for Lake Taihu," *IEEE J. Sel. Topics Appl. Earth Observ. Remote Sens.*, vol. 9, no. 2, pp. 793–803, Feb. 2015.

[22] M. Wang and L. Jiang, "Atmospheric correction using the information from the short blue band," *IEEE Trans. Geosci. Remote Sens.*, vol. 56, no. 10, pp. 6224–6237, Oct. 2018.

[23] H. Ye, C. Chen, and C. Yang, "Atmospheric correction of Landsat-8/OLI imagery in turbid estuarine waters: A case study for the Pearl River estuary," *IEEE J. Sel. Topics Appl. Earth Observ. Remote Sens.*, vol. 10, no. 1, pp. 252–261, Jan. 2016.

[24] N. Pahlevan, J.-C. Roger, and Z. Ahmad, "Revisiting short-wave-infrared (SWIR) bands for atmospheric correction in coastal waters," *Opt. Exp.*, vol. 25, no. 6, pp. 6015–6035, 2017.

[25] S. Bi *et al.*, "Inland water atmospheric correction based on turbidity classification using OLCI and SLSTR synergistic observations," *Remote Sens.*, vol. 10, no. 7, 2018, Art. no. 1002.

[26] S. B. Groom *et al.*, "Satellite ocean colour: Current status and future perspective," *Frontiers Mar. Sci.*, vol. 6, 2019, Art. no. 485, doi: 10.3389/fmars.2019.00485.

[27] X. Yu, H. Yi, X. Liu, Y. Wang, X. Liu, and H. Zhang, "Remote-sensing estimation of dissolved inorganic nitrogen concentration in the Bohai Sea using band combinations derived from MODIS data," *Int. J. Remote Sens.*, vol. 37, no. 2, pp. 327–340, 2016.

[28] L. Deng *et al.*, "Retrieving phytoplankton size class from the absorption coefficient and chlorophyll a concentration based on support vector machine," *Remote Sens.*, vol. 11, no. 9, 2019, Art. no. 1054.

[29] Z. Lee, K. L. Carder, and R. A. Arnone, "Deriving inherent optical properties from water color: A multiband quasi-analytical algorithm for optically deep waters," *Appl. Opt.*, vol. 41, no. 27, pp. 5755–5772, 2002.

[30] S. B. Groom *et al.*, "Satellite ocean colour: Current status and future perspective," *Frontiers Mar. Sci.*, vol. 6, 2019, Art. no. 485.

[31] W. Shi and M. Wang, "A blended inherent optical property algorithm for global satellite ocean color observations," *Limnol. Oceanogr. Methods*, vol. 17, no. 7, pp. 377–394, 2019.

[32] X. Huang *et al.*, "Evaluation of four atmospheric correction algorithms for GOCI images over the Yellow Sea," *Remote Sens.*, vol. 11, no. 14, 2019, Art. no. 1631.

[33] K. L. Carder, F. R. Chen, Z. Lee, S. K. Hawes, and J. P. Cannizzaro, "MODIS ocean science team algorithm theoretical basis document," ATBD 19 Case 2 Chlorophyll a, Version 7. 30, 2003.

[34] T. W. Cui *et al.*, "Remote sensing of chlorophyll a concentration in turbid coastal waters based on a global optical water classification system," *ISPRS J. Photogrammetry Remote Sens.*, vol. 163, pp. 187–201, 2020.

[35] Y.-S. Son and H. Kim, "Empirical ocean color algorithms and bio-optical properties of the western coastal waters of Svalbard, Arctic," *ISPRS J. Photogrammetry Remote Sens.*, vol. 139, pp. 272–283, 2018.

[36] J. E. O'Reilly and P. J. Werdell, "Chlorophyll algorithms for ocean color sensors - OC4, OC5 & OC6," *Remote Sens. Environ.*, vol. 229, pp. 32–47, Aug. 2019, doi: 10.1016/j.rse.2019.04.021.

[37] C. Hu, Z. Lee, and B. Franz, "Chlorophyll aalgorithms for oligotrophic oceans: A novel approach based on three-band reflectance difference," *J. Geophys. Res. Oceans*, vol. 117, no. C01011, 2012.

[38] C. Neil, E. Spyrakos, P. D. Hunter, and A. N. Tyler, "A global approach for chlorophyll-a retrieval across optically complex inland waters based on optical water types," *Remote Sens. Environ.*, vol. 229, pp. 159–178, 2019.

[39] J. Wei, Z. Lee, and S. Shang, "A system to measure the data quality of spectral remote-sensing reflectance of aquatic environments," *J. Geophys. Res. Oceans*, vol. 121, no. 11, pp. 8189–8207, 2016.

[40] T. Cui, J. Zhang, S. Groom, L. Sun, T. Smyth, and S. Sathyendranath, "Validation of MERIS ocean-color products in the Bohai Sea: A case study for turbid coastal waters," *Remote Sens. Environ.*, vol. 114, no. 10, pp. 2326–2336, 2010.

[41] P. J. Werdell *et al.*, "An overview of approaches and challenges for retrieving marine inherent optical properties from ocean color remote sensing," *Prog. Oceanogr.*, vol. 160, pp. 186–212, Jan. 2018, doi: 10.1016/j.pocean.2018.01.001.

[42] S. Parsons, M. Amani, and A. Moghimi, "Ocean colour mapping using remote sensing technology and an unsupervised machine learning algorithm," *J. Ocean Technol.*, vol. 16, no. 3, 2021, Art. no. 3. [Online]. Available: https://www.thejot.net/article-preview/?show_article_preview=1281

[43] M. Wang, "Remote sensing of the ocean contributions from ultraviolet to near-infrared using the shortwave infrared bands: Simulations," *Appl. Opt.*, vol. 46, no. 9, pp. 1535–1547, 2007.

[44] Z. Lee, J. Marra, M. J. Perry, and M. Kahru, "Estimating oceanic primary productivity from ocean color remote sensing: A strategic assessment," *J. Mar. Syst.*, vol. 149, pp. 59–59, Sep. 2015, doi: 10.1016/j.jmarsys.2014.11.015.

[45] D. B. Allison, D. Stramski, and B. G. Mitchell, "Seasonal and interannual variability of particulate organic carbon within the southern ocean from satellite ocean color observations," *J. Geophys. Res. Oceans*, vol. 115, no. C6, 2010.

[46] C. E. Del Castillo and R. L. Miller, "On the use of ocean color remote sensing to measure the transport of dissolved organic carbon by the Mississippi River Plume," *Remote Sens. Environ.*, vol. 112, no. 3, pp. 836–844, 2008.

[47] G. B. Brassington and P. Divakaran, "The theoretical impact of remotely sensed sea surface salinity observations in a multi-variate assimilation system," *Ocean Model.*, vol. 27, no. 1/2, pp. 70–81, 2009.

[48] S. Chen and C. Hu, "Estimating sea surface salinity in the northern Gulf of Mexico from satellite ocean color measurements," *Remote Sens. Environ.*, vol. 201, no. Feb., pp. 115–132, 2017, doi: 10.1016/j.rse.2017.09.004.

[49] B. Hassani, M. R. Sahebi, and R. M. Asiyabi, "Oil spill four-class classification using UAVSAR polarimetric data," *Ocean Sci. J.*, vol. 55, no. 3, pp. 433–443, 2020.

[50] W. Alpers, B. Holt, and K. Zeng, "Oil spill detection by imaging radars: Challenges and pitfalls," *Remote Sens. Environ.*, vol. 201, pp. 133–147, 2017.

[51] M. N. Jha, J. Levy, and Y. Gao, "Advances in remote sensing for oil spill disaster management: State-of-the-art sensors technology for oil spill surveillance," *Sensors*, vol. 8, no. 1, pp. 236–255, 2008.

[52] S.-H. Park, H.-S. Jung, and M.-J. Lee, "Oil spill mapping from Kompsat-2 high-resolution image using directional median filtering and artificial neural network," *Remote Sens.*, vol. 12, no. 2, 2020, Art. no. 253.

[53] Q. Bao, M. Lin, Y. Zhang, X. Dong, S. Lang, and P. Gong, "Ocean surface current inversion method for a Doppler scatterometer," *IEEE Trans. Geosci. Remote Sens.*, vol. 55, no. 11, pp. 6505–6516, Nov. 2017.

[54] G. S. E. Lagerloef, G. T. Mitchum, R. B. Lukas, and P. P. Niiler, "Tropical Pacific near-surface currents estimated from altimeter, wind, and drifter data," *J. Geophys. Res. Oceans*, vol. 104, no. C10, pp. 23313–23326, 1999.

[55] V. Klemas, "Remote sensing of coastal and ocean currents: An overview," *J. Coastal Res.*, vol. 28, no. 3, pp. 576–586, 2012.

[56] V. Kudryavtsev, M. Yurovskaya, B. Chapron, F. Collard, and C. Donlon, "Sun glitter imagery of ocean surface waves. Part 1: Directional spectrum retrieval and validation," *J. Geophys. Res. Oceans*, vol. 122, no. 2, pp. 1369–1383, 2017.

[57] M. Yurovskaya, V. Kudryavtsev, B. Chapron, and F. Collard, "Ocean surface current retrieval from space: The Sentinel-2 multispectral capabilities," *Remote Sens. Environ.*, vol. 234, 2019, Art. no. 111468, doi: 10.1016/j.rse.2019.111468.

[58] S. Sandven, O. M. Johannessen, and K. Kloster, "Sea ice monitoring by remote sensing," in *Encyclopedia of Analytical Chemistry*. Hoboken, NJ, USA: Wiley, 2006.

[59] L. Ning *et al.*, "Using remote sensing to estimate sea ice thickness in the Bohai Sea, China based on ice type," *Int. J. Remote Sens.*, vol. 30, no. 17, pp. 4539–4552, 2009.

[60] M. Liu, Y. Dai, J. Zhang, X. Zhang, J. Meng, and Q. Xie, "PCA-based sea-ice image fusion of optical data by HIS transform and SAR data by wavelet transform," *Acta Oceanol. Sinica*, vol. 34, no. 3, pp. 59–67, 2015.

[61] H. Su, B. Ji, and Y. Wang, "Sea ice extent detection in the Bohai Sea using Sentinel-3 OLCI data," *Remote Sens.*, vol. 11, no. 20, 2019, Art. no. 2436.

[62] C. Zhao, C.-Z. Qin, and J. Teng, "Mapping large-area tidal flats without the dependence on tidal elevations: A case study of Southern China," *ISPRS J. Photogrammetry Remote Sens.*, vol. 159, pp. 256–270, 2020.

[63] C. Small and R. J. Nicholls, "A global analysis of human settlement in coastal zones," *J. Coastal Res.*, vol. 19, no. 3, pp. 584–599, 2003.

[64] E. B. Barbier, S. D. Hacker, C. Kennedy, E. W. Koch, A. C. Stier, and B. R. Silliman, "The value of estuarine and coastal ecosystem services," *Ecological Monographs*, vol. 81, no. 2, pp. 169–193, 2011.

[65] K. Zhang, X. Dong, Z. Liu, W. Gao, Z. Hu, and G. Wu, "Mapping tidal flats with Landsat 8 images and google Earth engine: A case study of the China's Eastern Coastal zone circa 2015," *Remote Sens.*, vol. 11, no. 8, 2019, Art. no. 924.

[66] U. Kanjir, H. Greidanus, and K. Oštir, "Vessel detection and classification from spaceborne optical images: A literature survey," *Remote Sens. Environ.*, vol. 207, pp. 1–26, Mar. 2018, doi: 10.1016/j.rse.2017.12.033.

[67] Q. Xing, R. Meng, M. Lou, L. Bing, and X. Liu, "Remote sensing of ships and offshore oil platforms and mapping the marine oil spill risk source in the Bohai Sea," *Aquatic Procedia*, vol. 3, pp. 127–132, 2015.

[68] Q. Li, L. Mou, Q. Liu, Y. Wang, and X. X. Zhu, "HSF-Net: Multiscale deep feature embedding for ship detection in optical remote sensing imagery," *IEEE Trans. Geosci. Remote Sens.*, vol. 56, no. 12, pp. 7147–7161, Dec. 2018.

[69] E. P. Green *et al.*, *World Atlas of Seagrasses*. Berkeley, CA, USA: Univ. California Press, 2003.

[70] M. Amani, C. Macdonald, S. Mahdavi, M. Gullage, and J. So, "Aquatic vegetation mapping using machine learning algorithms and bathymetric lidar data: A case study from Newfoundland, Canada," *J. Ocean Technol.*, vol. 16, no. 3, 2021, Art. no. 74. [Online]. Available: https://www.thejot.net/article-preview/?show_article_preview=1278

[71] L. M. Nordlund, E. W. Koch, E. B. Barbier, and J. C. Creed, "Seagrass ecosystem services and their variability across genera and geographical regions," *PLoS One*, vol. 11, no. 10, 2016, Art. no. e0163091.

[72] D. Traganos, B. Aggarwal, D. Poursanidis, K. Topouzelis, N. Chrysoulakis, and P. Reinartz, "Towards global-scale seagrass mapping and monitoring using Sentinel-2 on Google Earth Engine: The case study of the Aegean and Ionian Seas," *Remote Sens.*, vol. 10, no. 8, Aug. 2018, Art. no. 1227, doi: 10.3390/rs10081227.

[73] I. Caballero and R. P. Stumpf, "Retrieval of nearshore bathymetry from Sentinel-2A and 2B satellites in South Florida Coastal waters," *Estuarine, Coastal, Shelf Sci.*, vol. 226, 2019, Art. no. 106277.

[74] G. Casal, X. Monteys, J. Hedley, P. Harris, C. Cahalane, and T. McCarthy, "Assessment of empirical algorithms for bathymetry extraction using Sentinel-2 data," *Int. J. Remote Sens.*, vol. 40, no. 8, pp. 2855–2879, 2019.

[75] A. G. Dekker *et al.*, "Intercomparison of shallow water bathymetry, hydro-optics, and Benthos mapping techniques in Australian and Caribbean coastal environments," *Limnol. Oceanogr. Methods*, vol. 9, no. 9, pp. 396–425, 2011.

[76] R. P. Stumpf, K. Holderied, and M. Sinclair, "Determination of water depth with high-resolution satellite imagery over variable bottom types," *Limnol. Oceanogr.*, vol. 48, no. 1, (pt. 2), pp. 547–556, 2003.

[77] M. Planck, "On the law of distribution of energy in the normal spectrum," *Ann. Phys.*, vol. 4, no. 553, 1901.

[78] P. J. Minnett *et al.*, "Half a century of satellite remote sensing of sea-surface temperature," *Remote Sens. Environ.*, vol. 233, 2019, Art. no. 111366.

[79] H. Lee, J.-S. Won, and W. Park, "An atmospheric correction using high resolution numerical weather prediction models for satellite-borne single-channel mid-wavelength and thermal infrared imaging sensors," *Remote Sens.*, vol. 12, no. 5, 2020, Art. no. 853.

[80] B. Tardy, V. Rivalland, M. Huc, O. Hagolle, S. Marcq, and G. Boulet, "A software tool for atmospheric correction and surface temperature estimation of Landsat infrared thermal data," *Remote Sens.*, vol. 8, no. 9, 2016, Art. no. 696.

[81] C. J. Merchant and P. L. Borgne, "Retrieval of sea surface temperature from space, based on modeling of infrared radiative transfer: Capabilities and limitations," *J. Atmos. Ocean. Technol.*, vol. 21, no. 11, pp. 1734–1746, 2004.

[82] B. Petrenko, A. Ignatov, Y. Kihai, and A. Heidinger, "Clear-sky mask for the advanced clear-sky processor for oceans," *J. Atmos. Ocean. Technol.*, vol. 27, no. 10, pp. 1609–1623, 2010.

[83] C. J. Merchant, A. R. Harris, E. Maturi, and S. MacCallum, "Probabilistic physically based cloud screening of satellite infrared imagery for operational sea surface temperature retrieval," *Quart. J. Roy. Meteorological Soc.*, vol. 131, no. 611, pp. 2735–2755, 2005.

[84] K. A. Kilpatrick, G. Podestá, E. Williams, S. Walsh, and P. J. Minnett, "Alternating decision trees for cloud masking in MODIS and VIIRS NASA sea surface temperature products," *J. Atmos. Ocean. Technol.*, vol. 36, no. 3, pp. 387–407, 2019.

[85] I. J. Barton, "Satellite-derived sea surface temperatures: Current status," *J. Geophys. Res. Oceans*, vol. 100, no. C5, pp. 8777–8790, 1995.

[86] L. M. McMillin and D. S. Crosby, "Some physical interpretations of statistically derived coefficients for split-window corrections to satellite-derived sea surface temperatures," *Quart. J. Roy. Meteorological Soc.*, vol. 111, no. 469, pp. 867–871, 1985.

[87] S. Martin, *An Introduction to Ocean Remote Sensing*. Cambridge, U.K.: Cambridge Univ. Press, 2014.

[88] K. A. Kilpatrick *et al.*, "A decade of sea surface temperature from MODIS," *Remote Sens. Environ.*, vol. 165, pp. 27–41, 2015.

[89] J. Fu, C. Chen, B. Guo, Y. Chu, and H. Zheng, "A split-window method to retrieving sea surface temperature from Landsat 8 thermal infrared remote sensing data in offshore waters," *Estuarine, Coastal, Shelf Sci.*, vol. 236, 2020, Art. no. 106626.

[90] C. J. Merchant, P. L. Borgne, A. Marsouin, and H. Roquet, "Optimal estimation of sea surface temperature from split-window observations," *Remote Sens. Environ.*, vol. 112, no. 5, pp. 2469–2484, 2008.

[91] B.-H. Tang, "Nonlinear split-window algorithms for estimating land and sea surface temperatures from simulated Chinese Gaofen-5 satellite data," *IEEE Trans. Geosci. Remote Sens.*, vol. 56, no. 11, pp. 6280–6289, Nov. 2018.

[92] B. Petrenko, A. Ignatov, Y. Kihai, J. Stroup, and P. Dash, "Evaluation and selection of SST regression algorithms for JPSS VIIRS," *J. Geophys. Res. Atmos.*, vol. 119, no. 8, pp. 4580–4599, 2014.

[93] D. T. Llewellyn-Jones, P. J. Minnett, R. W. Saunders, and A. M. Zavody, "Satellite multichannel infrared measurements of sea surface temperature of the NE Atlantic Ocean using AVHRR/2," *Quart. J. Roy. Meteorological Soc.*, vol. 110, no. 465, pp. 613–631, 1984.

[94] X. Meng and J. Cheng, "Estimating land and sea surface temperature from cross-calibrated Chinese Gaofen-5 thermal infrared data using split-window algorithm," *IEEE Geosci. Remote Sens. Lett.*, vol. 17, no. 3, pp. 509–513, Mar. 2019.

[95] P. J. Minnett, J. R. Eyre, and R. W. Pescod, "The variability of the North Atlantic marine atmosphere and its relevance to remote sensing," *Int. J. Remote Sens.*, vol. 8, no. 6, pp. 871–880, 1987.

[96] S. L. Haines, G. J. Jedlovec, and S. M. Lazarus, "A MODIS sea surface temperature composite for regional applications," *IEEE Trans. Geosci. Remote Sens.*, vol. 45, no. 9, pp. 2919–2927, Sep. 2007.

[97] R. D. Putra *et al.*, "Detection of reef scale thermal stress with Aqua and Terra MODIS satellite for coral bleaching phenomena," *AIP Conf. Proc.*, vol. 2094, no. 1, 2019, Art. no. 20024.

[98] D. Yuan, J. Zhu, C. Li, and D. Hu, "Cross-shelf circulation in the Yellow and East China Seas indicated by MODIS satellite observations," *J. Mar. Syst.*, vol. 70, no. 1/2, pp. 134–149, 2008.

[99] S. J. Goodman, "GOES-R series introduction," in *The GOES-R Series*. Amsterdam, The Netherlands: Elsevier, 2020, pp. 1–3.

[100] J. Ji, J. Ma, C. Dong, J. C. H. Chiang, and D. Chen, "Regional dependence of atmospheric responses to Oceanic Eddies in the North Pacific Ocean," *Remote Sens.*, vol. 12, no. 7, 2020, Art. no. 1161.

[101] B. S. Ferster, B. Subrahmanyam, and A. M. Macdonald, "Confirmation of ENSO-Southern Ocean teleconnections using satellite-derived SST," *Remote Sens.*, vol. 10, no. 2, 2018, Art. no. 331.

[102] A. Wirasatriya, R. Y. Setiawan, and P. Subardjo, "The effect of ENSO on the variability of chlorophyll-a and sea surface temperature in the Maluku Sea," *IEEE J. Sel. Topics Appl. Earth Observ. Remote Sens.*, vol. 10, no. 12, pp. 5513–5518, Dec. 2017.

[103] Y.-L. Wu, M.-A. Lee, L.-C. Chen, J.-W. Chan, and K.-W. Lan, "Evaluating a suitable aquaculture site selection model for cobia (Rachycentron canadum) during extreme events in the inner bay of the Penghu Islands, Taiwan," *Remote Sens.*, vol. 12, no. 17, 2020, Art. no. 2689.

[104] R. Mugo and S.-I. Saitoh, "Ensemble modelling of Skipjack tuna (Katsuwonus pelamis) habitats in the western North Pacific using satellite remotely sensed data; a comparative analysis using machine-learning models," *Remote Sens.*, vol. 12, no. 16, 2020, Art. no. 2591.

[105] R. A. B. Mason, W. J. Skirving, and S. G. Dove, "Integrating physiology with remote sensing to advance the prediction of coral bleaching events," *Remote Sens. Environ.*, vol. 246, 2020, Art. no. 111794.

[106] W. G. Large and S. G. Yeager, "On the observed trends and changes in global sea surface temperature and air–sea heat fluxes (1984–2006)," *J. Climate*, vol. 25, no. 18, pp. 6123–6135, 2012.

[107] C. J. Merchant et al., "Satellite-based time-series of sea-surface temperature since 1981 for climate applications," *Sci. Data*, vol. 6, no. 1, pp. 1–18, 2019.

[108] A. Pisano et al., "New evidence of Mediterranean climate change and variability from sea surface temperature observations," *Remote Sens.*, vol. 12, no. 1, p. 132, 2020.

[109] A. Olsen, J. A. Triñanes, and R. Wanninkhof, "Sea–air flux of CO2 in the Caribbean Sea estimated using in situ and remote sensing data," *Remote Sens. Environ.*, vol. 89, no. 3, pp. 309–325, 2004.

[110] M. Konda, N. Imasato, and A. Shibata, "Analysis of the global relationship of biennial variation of sea surface temperature and air-sea heat flux using satellite data," *J. Oceanogr.*, vol. 52, no. 6, pp. 717–746, 1996.

[111] K. A. Alawad, A. M. Al-Subhi, M. A. Alsaafani, and T. M. Alraddadi, "Atmospheric forcing of the high and low extremes in the sea surface temperature over the Red Sea and associated Chlorophyll-a concentration," *Remote Sens.*, vol. 12, no. 14, 2020, Art. no. 2227.

[112] R. Torres et al., "Sensitivity of modeled CO2 air–sea flux in a coastal environment to surface temperature gradients, surfactants, and satellite data assimilation," *Remote Sens.*, vol. 12, no. 12, 2020, Art. no. 2038.

[113] C. Xiao et al., "A spatiotemporal deep learning model for sea surface temperature field prediction using time-series satellite data," *Environ. Model. Softw.*, vol. 120, 2019, Art. no. 104502.

[114] A. C. Stuart-Menteth, I. S. Robinson, and P. G. Challenor, "A global study of diurnal warming using satellite-derived sea surface temperature," *J. Geophys. Res. Oceans*, vol. 108, 2003, Art. no. C5.

[115] X. Liu, D.-L. Zhang, and J. Guan, "Parameterizing sea surface temperature cooling induced by tropical cyclones: 2. Verification by ocean drifters," *J. Geophys. Res. Oceans*, vol. 124, no. 2, pp. 1232–1243, 2019.

[116] P. Katsafados, E. Mavromatidis, A. Papadopoulos, and I. Pytharoulis, "Numerical simulation of a deep mediterranean storm and its sensitivity on sea surface temperature," *Natural Hazards Earth Syst. Sci.*, vol. 11, no. 5, 2011, Art. no. 1233.

[117] J. Amelien, "Remote sensing of snow with passive microwave radiometers—A review of current algorithms," Report No. 1019, Oslo: Norsk Regnesentral, 2008.

[118] E. Ho, "Advanced microwave scanning radiometer (AMSR) SIPS." [Online]. Available: earthdata.nasa.gov

[119] D. Gayfulin, M. Tsyrulnikov, and A. Uspensky, "Assessment and adaptive correction of observations in atmospheric sounding channels of the satellite microwave radiometer MTVZA-GY," *Pure Appl. Geophys.*, vol. 175, no. 10, pp. 3653–3670, Oct. 2018, doi: 10.1007/s00024-018-1917-7.

[120] F. J. Wentz, "Measurement of oceanic wind vector using satellite microwave radiometers," *IEEE Trans. Geosci. Remote Sens.*, vol. 30, no. 5, pp. 960–972, May 1992.

[121] T. T. Wilheit, "Electrically scanning microwave radiometer (ESMR)," NASA Space Science Data Coordinated Archive, NASA, Washington, DC, USA. [Online]. Available: https://nssdc.gsfc.nasa.gov/nmc/experiment/display.action?id=1972-097A-04

[122] National Snow and Ice Data Center, NSIDC. [Online]. Available: https://nsidc.org/

[123] SMMR, SSM/I, and SSMIS Sensors, National Snow and Ice Data Center, 2018. [Online]. Available: https://nsidc.org/data/smmr_ssmi

[124] WMO OSCAR, Satellite: DMSP-F16, 2020. [Online]. Available: https://space.oscar.wmo.int/satellites/view/dmsp_f16

[125] SMOS - ESA Earth Observation Missions - Earth Online - ESA, European Space Agency. [Online]. Available: https://earth.esa.int/eogateway/missions/smos

[126] J. Font et al., "SMOS first data analysis for sea surface salinity determination," *Int. J. Remote Sens.*, vol. 34, no. 9, pp. 3654–3670, 2013, doi: 10.1080/01431161.2012.716541.

[127] P. W. Gaiser et al., "The WindSat spaceborne polarimetric microwave radiometer: Sensor description and early orbit performance," *IEEE Trans. Geosci. Remote Sens.*, vol. 42, no. 11, pp. 2347–2361, Nov. 2004.

[128] W. J. Wilson, S. J. Dinardo, and S. V. Hsiao, "Polarimetric microwave wind radiometer model function and retrieval testing for WindSat," *IEEE Trans. Geosci. Remote Sens.*, vol. 44, no. 3, pp. 584–595, Mar. 2006.

[129] S. Hong and I. Shin, "Wind speed retrieval based on sea surface roughness measurements from spaceborne microwave radiometers," *J. Appl. Meteorol. Climatol.*, vol. 52, no. 2, pp. 507–516, Feb. 2013, doi: 10.1175/JAMC-D-11-0209.1.

[130] R. Lumpkin and M. Pazos, "Measuring surface currents with surface velocity program drifters: The instrument, its data, and some recent results," in *Proc. Lagrangian Anal. Prediction Coastal Ocean Dyn.*, vol. 2, pp. 39–67, 2007.

[131] S. L. Castro, G. A. Wick, and W. J. Emery, "Evaluation of the relative performance of sea surface temperature measurements from different types of drifting and moored buoys using satellite-derived reference products," *J. Geophys. Res. Oceans*, vol. 117, no. 2, 2012, Art. no. C02029, doi: 10.1029/2011JC007472.

[132] C. J. Donlon et al., "Toward improved validation of satellite sea surface skin temperature measurements for climate research," *J. Climate*, vol. 15, pp. 353–369, 2002, doi: 10.1175/1520-0442(2002)015<0353:TIVOSS>2.0.CO;2.

[133] R. Branch, A. T. Jessup, and R. Branch, "Integrated ocean skin and bulk temperature measurements using the calibrated infrared in situ measurement system (CIRIMS) and through-hull ports," *J. Atmos. Ocean. Technol.*, vol. 25, pp. 579–597, 2008, doi: 10.1175/2007JTECHO479.1.

[134] P. J. Minnett, M. Smith, and B. Ward, "Measurements of the oceanic thermal skin effect," *Deep-Sea Res. Part II Top. Stud. Oceanogr.*, vol. 58, no. 6, pp. 861–868, Mar. 2011, doi: 10.1016/j.dsr2.2010.10.024.

[135] B. Ward and M. A. Donelan, "Thermometric measurements of the molecular sublayer at the air-water interface," *Geophys. Res. Lett.*, vol. 33, no. 7, p. L07605, Apr. 2006, doi: 10.1029/2005GL024769.

[136] Y. Wu, M. Li, Y. Bao, and G. P. Petropoulos, "Cross-validation of radio-frequency-interference signature in satellite microwave radiometer observations over the ocean," *Remote Sens.*, vol. 12, no. 20, Oct. 2020, Art. no. 3433, doi: 10.3390/rs12203433.

[137] C. L. Gentemann, "Three way validation of MODIS and AMSR-E sea surface temperatures," *J. Geophys. Res. Oceans*, vol. 119, no. 4, pp. 2583–2598, Apr. 2014, doi: 10.1002/2013JC009716.

[138] A. G. O'carroll, J. R. Eyre, and R. W. Saunders, "Three-way error analysis between AATSR, AMSR-E, and in situ sea surface temperature observations," *J. Atmos. Ocean. Technol.*, vol. 25, no. 7, pp. 1197–1207, 2008, doi: 10.1175/2007JTECHO542.1.

[139] C. González-Haro and J. Isern-Fontanet, "Assessment of ocean surface currents reconstruction at a global scale from the synergy between microwave and altimetric measurements," in *Proc. Int. Geosci. Remote Sens. Symp.*, 2013, pp. 2950–2953, doi: 10.1109/IGARSS.2013.6723444.

[140] G. Lagerloef and J. Font, "SMOS and aquarius/SAC-D missions: The era of spaceborne salinity measurements is about to begin," in *Oceanography From Space: Revisited*. Dordrecht, The Netherlands: Springer, 2010, pp. 35–58.

[141] S. H. Yueh, R. West, W. J. Wilson, F. K. Li, E. G. Njoku, and Y. Rahmat-Samii, "Error sources and feasibility for microwave remote sensing of ocean surface salinity," *IEEE Trans. Geosci. Remote Sens.*, vol. 39, no. 5, pp. 1049–1060, May 2001.

[142] D. M. L. Vine, J. B. Zaitzeff, E. J. D'Sa, J. L. Miller, C. Swift, and M. Goodberlet, "Chapter 19 Sea surface salinity: Toward an operational remote-sensing system," *Elsevier Oceanogr. Ser.*, vol. 63, no. C, pp. 321–335, Jan. 2000, doi: 10.1016/S0422-9894(00)80020-3.

[143] J. Font, A. Camps, and J. Ballabrera-Poy, "Microwave aperture synthesis radiometry: Paving the path for sea surface salinity measurement from space," in *Remote Sensing of the European Seas*. Dordrecht, The Netherlands: Springer, 2008, pp. 223–238.

[144] J. Font *et al.*, "SMOS: The challenging sea surface salinity measurement from space," *Proc. IEEE*, vol. 98, no. 5, pp. 649–665, May 2010, doi: 10.1109/JPROC.2009.2033096.

[145] K. D. McMullan *et al.*, "SMOS: The payload," *IEEE Trans. Geosci. Remote Sens.*, vol. 46, no. 3, pp. 594–605, Mar. 2008.

[146] X. Yin, J. Boutin, E. Dinnat, Q. Song, and A. Martin, "Roughness and foam signature on SMOS-MIRAS brightness temperatures: A semi-theoretical approach," *Remote Sens. Environ.*, vol. 180, pp. 221–233, Jul. 2016, doi: 10.1016/j.rse.2016.02.005.

[147] J. Boutin, J. L. Vergely, S. Marchand, N. Kolodziejczyk, and N. Reul, "Revised mitigation of systematic errors in SMOS sea surface salinity," in *Proc. Int. Geosci. Remote Sens. Symp.*, Oct. 2018, pp. 5640–5643, doi: 10.1109/IGARSS.2018.8519011.

[148] J. Boutin *et al.*, "New SMOS sea surface salinity with reduced systematic errors and improved variability," *Remote Sens. Environ.*, vol. 214, pp. 115–134, Sep. 2018, doi: 10.1016/j.rse.2018.05.022.

[149] Pi-MEP, "Match-up database analyses report," SMAP SSS L3 v5.0, 2019. [Online]. Available: https://pimep.ifremer.fr/diffusion/analyses/mdb-database/SCS/smap-l3-jpl-v5.0-8dr/tsg-samos/report/pimep-mdb-report_SCS_smap-l3-jpl-v5.0-8dr_tsg-samos_20201215.pdf

[150] N. Reul *et al.*, "Sea surface salinity estimates from spaceborne L-band radiometers : An overview of the fi rst decade of observation (2010–2019)," *Remote Sens. Environ.*, vol. 242, 2020, Art. no. 111769, doi: 10.1016/j.rse.2020.111769.

[151] P. Rostosky, G. Spreen, S. L. Farrell, T. Frost, G. Heygster, and C. Melsheimer, "Snow depth retrieval on Arctic Sea ice from passive microwave radiometers—Improvements and extensions to multiyear ice using lower frequencies," *J. Geophys. Res. Oceans*, vol. 123, no. 10, pp. 7120–7138, Oct. 2018, doi: 10.1029/2018JC014028.

[152] P. W. Gaiser, "WindSat-satellite-based polarimetric microwave radiometer," in *Proc. IEEE MTT-S Int. Microw. Symp. Dig.*, vol. 1 pp. 403–406, 1999.

[153] L. Tsang, J. A. Kong, and R. T. Shin, *Theory of Microwave Remote Sensing*. Cambridge, MA, USA: MIT Press, 1985.

[154] P. S. Narvekar, G. Heygster, R. Tonboe, and T. J. Jackson, "Analysis of WindSat data over Arctic Sea ice," in *Proc. IEEE Int. Geosci. Remote Sens. Symp.*, vol. 5, pp. V369–V372, 2008.

[155] P. W. Gaiser, K. M. St Germain, and E. M. Twarog, "WindSat-spaceborne remote sensing of ocean surface winds," in *Proc. Celebrating Past Teaming Toward Future*, vol. 1, p. 208, 2003.

[156] W. L. Jones, J. D. Park, S. Soisuvarn, L. Hong, P. W. Gaiser, and K. M. S. Germain, "Deep-space calibration of the WindSat radiometer," *IEEE Trans. Geosci. Remote Sens.*, vol. 44, no. 3, pp. 476–495, Mar. 2006.

[157] F. J. Wentz, L. Ricciardulli, C. Gentemann, T. Meissner, K.A. Hilburn, and J. Scott, "Remote Sensing Systems Coriolis WindSat Environmental Suite on 0.25 deg grid, Version 7.0.1," *Remote Sens. Syst.*, Santa Rosa, CA, 2013. [Online]. Available: www.remss.com/missions/windsat

[158] T. Meissner and F. J. Wentz, "Wind-vector retrievals under rain with passive satellite microwave radiometers," *IEEE Trans. Geosci. Remote Sens.*, vol. 47, no. 9, pp. 3065–3083, Sep. 2009.

[159] T. Meissner and F. Wentz, "Ocean retrievals for windsat: Radiative transfer model, algorithm, validation," in *Proc. OCEANS MTS/IEEE*, 2005, pp. 130–133.

[160] L. Zhang, X. Yin, H. Shi, and Z. Wang, "Hurricane wind speed estimation using WindSat 6 and 10 GHz brightness temperatures," *Remote Sens.*, vol. 8, no. 9, p. 721, 2016, doi: 10.3390/rs8090721.

[161] M. Zheng, X.-M. Li, and J. Sha, "Comparison of sea surface wind field measured by HY-2A scatterometer and WindSat in global oceans," *J. Oceanol. Limnol.*, vol. 37, no. 1, pp. 38–46, 2019.

[162] V. U. Zavorotny, S. Gleason, E. Cardellach, and A. Camps, "Tutorial on remote sensing using GNSS bistatic radar of opportunity," *IEEE Geosci. Remote Sens. Mag.*, vol. 2, no. 4, pp. 8–45, Apr. 2014.

[163] M. Martin-Neira *et al.*, "A passive reflectometry and interferometry system (PARIS): Application to ocean altimetry," *ESA J.*, vol. 17, no. 4, pp. 331–355, 1993.

[164] C. D. Hall and R. A. Cordey, "Multistatic scatterometry," in *Proc. Int. Geosci. Remote Sens. Symp., "Remote Sens.: Moving Toward 21st Century,"* 1988, pp. 561–562, doi: 10.1109/igarss.1988.570200.

[165] J. L. Garrison, S. J. Katzberg, and M. I. Hill, "Effect of sea roughness on bistatically scattered range coded signals from the global positioning system," *Geophys. Res. Lett.*, vol. 25, no. 13, pp. 2257–2260, 1998, doi: 10.1029/98gl51615.

[166] B. Lin, S. J. Katzberg, J. L. Garrison, and B. A. Wielicki, "Relationship between GPS signals reflected from sea surfaces and surface winds: Modeling results and comparisons with aircraft measurements," *J. Geophys. Res. Oceans*, vol. 104, no. C9, pp. 20713–20727, 1999, doi: 10.1029/1999jc900176.

[167] S. T. Lowe, J. L. LaBrecque, C. Zuffada, L. J. Romans, L. E. Young, and G. A. Hajj, "First spaceborne observation of an Earth-reflected GPS signal," *Radio Sci.*, vol. 37, no. 1, pp. 7–28, 2002, doi: 10.1029/2000rs002539.

[168] G. Beyerle, "GPS radio occultations with CHAMP: A radio holographic analysis of GPS signal propagation in the troposphere and surface reflections," *J. Geophys. Res.*, vol. 107, p. D24, 2002, doi: 10.1029/2001jd001402.

[169] G. Beyerle and K. Hocke, "Observation and simulation of direct and reflected GPS signals in radio occultation experiments," *Geophys. Res. Lett.*, vol. 28, no. 9, pp. 1895–1898, 2001, doi: 10.1029/2000gl012530.

[170] V. U. Zavorotny and A. G. Voronovich, "Scattering of GPS signals from the ocean with wind remote sensing application," *IEEE Trans. Geosci. Remote Sens.*, vol. 38, no. 2, pp. 951–964, Feb. 2000.

[171] T. Elfouhaily, B. Chapron, K. Katsaros, and D. Vandemark, "A unified directional spectrum for long and short wind-driven waves," *J. Geophys. Res. Oceans*, vol. 102, no. C7, pp. 15781–15796, 1997, doi: 10.1029/97jc00467.

[172] C. Cox and W. Munk, "Measurement of the roughness of the sea surface from photographs of the Sun's glitter," *J. Opt. Soc. Amer.*, vol. 44, no. 11, pp. 838–850, 1954, doi: 10.1364/josa.44.000838.

[173] M. P. Clarizia, C. S. Ruf, P. Jales, and C. Gommenginger, "Spaceborne GNSS-R minimum variance wind speed estimator," *IEEE Trans. Geosci. Remote Sens.*, vol. 52, no. 11, pp. 6829–6843, Nov. 2014.

[174] J. L. Garrison, A. Komjathy, V. U. Zavorotny, and S. J. Katzberg, "Wind speed measurement using forward scattered GPS signals," *IEEE Trans. Geosci. Remote Sens.*, vol. 40, no. 1, pp. 50–65, Jan. 2002.

[175] A. G. Voronovich and V. U. Zavorotny, "Bistatic radar equation for signals of opportunity revisited," *IEEE Trans. Geosci. Remote Sens.*, vol. 56, no. 4, pp. 1959–1968, Apr. 2018.

[176] S. Gleason *et al.*, "Detection and processing of bistatically reflected GPS signals from low Earth orbit for the purpose of ocean remote sensing," *IEEE Trans. Geosci. Remote Sens.*, vol. 43, no. 6, pp. 1229–1241, Jun. 2005.

[177] M. Unwin *et al.*, "GNSS enabling new capabilities in space on the TechDemoSat-1 satellite," *Proc. 30th Int. Tech. Meeting Satell. Division Inst. Navig.*, 2017, pp. 4066–4079, doi: 10.33012/2017.15349.

[178] M. Unwin, P. Jales, J. Tye, C. Gommenginger, G. Foti, and J. Rosello, "Spaceborne GNSS-reflectometry on TechDemoSat-1: Early mission operations and exploitation," *IEEE J. Sel. Topics Appl. Earth Observ. Remote Sens.*, vol. 9, no. 10, pp. 4525–4539, Oct. 2016.

[179] M. Asgarimehr, J. Wickert, and S. Reich, "TDS-1 GNSS reflectometry: Development and validation of forward scattering winds," *IEEE J. Sel. Topics Appl. Earth Observ. Remote Sens.*, vol. 11, no. 11, pp. 4534–4541, Nov. 2018.

[180] G. Foti *et al.*, "Spaceborne GNSS reflectometry for ocean winds: First results from the U.K. TechDemoSat-1 mission," *Geophys. Res. Lett.*, vol. 42, no. 13, pp. 5435–5441, 2015, doi: 10.1002/2015GL064204.

[181] G. Foti, C. Gommenginger, and M. Srokosz, "First spaceborne GNSS-reflectometry observations of hurricanes from the U.K. TechDemoSat-1 mission," *Geophys. Res. Lett.*, vol. 44, pp. 12358–12366, 2017, doi: 10.1002/2017gl076166.

[182] C. S. Ruf *et al.*, "A new paradigm in earth environmental monitoring with the CYGNSS small satellite constellation," *Sci. Rep.*, vol. 8, pp. 1–13, 2018, doi: 10.1038/s41598-018-27127-4.

[183] M. Asgarimehr, J. Wickert, and S. Reich, "Evaluating impact of rain attenuation on space-borne GNSS reflectometry wind speeds," *Remote Sens.,* vol. 11, no. 9, 2019, Art. no. 1048, doi: 10.3390/rs11091048.

[184] J. Wickert *et al.*, "GEROS-ISS: GNSS reflectometry, radio occultation, and scatterometry onboard the International Space Station," *IEEE J. Sel. Topics Appl. Earth Observ. Remote Sens.*, vol. 9, no. 10, pp. 4552–4581, Oct. 2016.

[185] E. Cardellach *et al.*, "GNSS Transpolar Earth Reflectometry exploriNg system (G-TERN): Mission concept," *IEEE Access*, vol. 6, pp. 13980–14018, 2018, doi: 10.1109/ACCESS.2018.2814072.

[186] S. Gleason, "Space-based GNSS scatterometry: Ocean wind sensing using an empirically calibrated model," *IEEE Trans. Geosci. Remote Sens.*, vol. 51, no. 9, pp. 4853–4863, Sep. 2013.

[187] C. S. Ruf, S. Gleason, and D. S. McKague, "Assessment of CYGNSS wind speed retrieval uncertainty," *IEEE J. Sel. Topics Appl. Earth Observ. Remote Sens.*, vol. 12, no. 1, pp. 87–97, Jan. 2019.

[188] Z. Cui, Z. Pu, V. Tallapragada, R. Atlas, and C. S. Ruf, "A preliminary impact study of CYGNSS ocean surface wind speeds on numerical simulations of hurricanes," *Geophys. Res. Lett.*, vol. 46, no. 5, pp. 2984–2992, 2019, doi: 10.1029/2019gl082236.

[189] C. Li and W. Huang, "An algorithm for sea-surface wind field retrieval from GNSS-R delay-Doppler map," *IEEE Geosci. Remote Sens. Lett.*, vol. 11, no. 12, pp. 2110–2114, Dec. 2014.

[190] M. Asgarimehr, I. Zhelavskaya, G. Foti, S. Reich, and J. Wickert, "A GNSS-R geophysical model function: Machine learning for wind speed retrievals," *IEEE Geosci. Remote Sens. Lett.*, vol. 17, no. 8, pp. 1333–1337, Aug. 2020.

[191] J. Reynolds, M. P. Clarizia, and E. Santi, "Wind speed estimation from CYGNSS using artificial neural networks," *IEEE J. Sel. Topics Appl. Earth Observ. Remote Sens.*, vol. 13, pp. 708–716, 2020, doi: 10.1109/jstars.2020.2968156.

[192] Y. Liu, I. Collett, and Y. J. Morton, "Application of neural network to GNSS-R wind speed retrieval," *IEEE Trans. Geosci. Remote Sens.*, vol. 57, no. 12, pp. 9756–9766, Dec. 2019.

[193] M. Wiehl, B. Legrésy, and R. Dietrich, "Potential of reflected GNSS signals for ice sheet remote sensing," *Prog. Electromagn. Res.*, vol. 40, pp. 177–205, 2003, doi: 10.2528/pier02102202.

[194] S. Gleason, "Remote sensing of ocean, ice and land surfaces using bistatically scattered GNSS signals from low earth orbit," PhD thesis, Univ. Surrey, Guildford, U.K., 2006, doi: 10.1109/JSTARS.2020.2966880.

[195] S. Gleason, "Towards sea ice remote sensing with space detected GPS signals: Demonstration of technical feasibility and initial consistency check using low resolution sea ice information," *Remote Sens.*, vol. 2, no. 8, pp. 2017–2039, 2010, doi: 10.3390/rs2082017.

[196] A. Alonso-Arroyo, V. U. Zavorotny, and A. Camps, "Sea ice detection using U.K. TDS-1 GNSS-R data," *IEEE Trans. Geosci. Remote Sens.*, vol. 55, no. 9, pp. 4989–5001, Sep. 2017.

[197] Q. Yan and W. Huang, "Detecting sea ice from TechDemoSat-1 data using support vector machines with feature selection," *IEEE J. Sel. Topics Appl. Earth Observ. Remote Sens.*, vol. 12, no. 5, pp. 1409–1416, 2019, doi: 10.1109/JSTARS.2019.2907008.

[198] Q. Yan and W. Huang, "Sea ice thickness measurement using spaceborne GNSS-R: First results with TechDemoSat-1 data," *IEEE J. Sel. Topics Appl. Earth Observ. Remote Sens.*, vol. 13, pp. 577–587, 2020.

[199] Y. Zhu, T. Tao, J. Zou, K. Yu, J. Wickert, and M. Semmling, "Spaceborne GNSS reflectometry for retrieving sea ice concentration using TDS-1 data," *IEEE Geosci. Remote Sens. Lett.*, vol. 18, no. 4, pp. 612–616, Nov. 2021.

[200] W. Li, E. Cardellach, F. Fabra, S. Ribo, and A. Rius, "Assessment of spaceborne GNSS-R ocean altimetry performance using CYGNSS mission raw data," *IEEE Trans. Geosci. Remote Sens.*, vol. 58, no. 1, pp. 238–250, Jan. 2020.

[201] M. P. Clarizia, C. Ruf, P. Cipollini, and C. Zuffada, "First spaceborne observation of sea surface height using GPS-reflectometry," *Geophys. Res. Lett.*, vol. 43, no. 2, pp. 767–774, 2016.

[202] W. Li, E. Cardellach, F. Fabra, A. Rius, S. Ribó, and M. Martín-Neira, "First spaceborne phase altimetry over sea ice using TechDemoSat-1 GNSS-R signals," *Geophys. Res. Lett.*, vol. 44, no. 16, pp. 8369–8376, 2017, doi: 10.1002/2017gl074513.

[203] J. Mashburn, P. Axelrad, S. T. Lowe, and K. M. Larson, "Global ocean altimetry with GNSS reflections from TechDemoSat-1," *IEEE Trans. Geosci. Remote Sens.*, vol. 56, no. 7, pp. 4088–4097, Jul. 2018.

[204] A. M. Semmling *et al.*, "Sea surface topography retrieved from GNSS reflectometry phase data of the GEOHALO flight mission," *Geophys. Res. Lett.*, vol. 41, no. 3, pp. 954–960, 2014, doi: 10.1002/2013gl058725.

[205] G. Ruffini, F. Soulat, M. Caparrini, O. Germain, and M. Martín-Neira, "The eddy experiment: Accurate GNSS-R ocean altimetry from low altitude aircraft," *Geophys. Res. Lett.*, vol. 31, no. 12, 2004, Art. no. L12306, doi: 10.1029/2004gl019994.

[206] M. Hoseini, M. Asgarimehr, V. Zavorotny, H. Nahavandchi, C. Ruf, and J. Wickert, "First evidence of mesoscale ocean eddies signature in GNSS reflectometry measurements," *Remote Sens.,* vol. 12, no. 3, p. 542, 2020, doi: 10.3390/rs12030542.

[207] M. Asgarimehr, V. Zavorotny, J. Wickert, and S. Reich, "Can GNSS reflectometry detect precipitation over oceans?," *Geophys. Res. Lett.*, vol. 45, no. 22, pp. 12512–585592, 2018, doi: 10.1029/2018gl079708.

[208] M. Asgarimehr *et al.*, "Remote sensing of precipitation using reflected GNSS signals: Response analysis of polarimetric observations," in *Proc. IEEE Trans. Geosci. Remote Sens.*, vol. 60, 2022, Art. no. 5800412, doi: 10.1109/TGRS.2021.3062492.

[209] H. Carreno-Luengo *et al.*, "3Cat-2—An experimental nanosatellite for GNSS-R earth observation: Mission concept and analysis," *IEEE J. Sel. Topics Appl. Earth Observ. Remote Sens.*, vol. 9, no. 10, pp. 4540–4551, Oct. 2016.

[210] C. Jing, X. Niu, C. Duan, F. Lu, G. Di, and X. Yang, "Sea surface wind speed retrieval from the first Chinese GNSS-R mission: Technique and preliminary results," *Remote Sens.,* vol. 11, no. 24, 2019, Art. no. 3013, doi: 10.3390/rs11243013.

[211] D. Masters *et al.*, "First results from the spire GNSS-R payload CubeSat missions," *AGUFM*, vol. 2019, pp. G14A–G106, 2019.

[212] Y. Sun *et al.*, "The status and progress of Fengyun-3e GNOS II mission for GNSS remote sensing," in *Proc. IEEE Int. Geosci. Remote Sens. Symp.*, Jul. 2019, pp. 5181–5184.

[213] A. Camps *et al.*, "Fsscat, the 2017 Copernicus masters' 'ESA Sentinel small satellite challenge' winner: A federated polar and soil moisture tandem mission based on 6U Cubesats," in *Proc. IEEE Int. Geosci. Remote Sens. Symp.*, 2018, pp. 8285–8287.

[214] A. Dielacher *et al.*, "The ESA passive reflectometry and dosimetry (PRETTY) mission," in *Proc. IEEE Int. Geosci. Remote Sens. Symp.*, 2019, pp. 5173–5176.

[215] J.-C. Juang, Y.-F. Tsai, and C.-T. Lin, "FORMOSAT-7R mission for GNSS reflectometry," in *Proc. IEEE Int. Geosci. Remote Sens. Symp.*, 2019, pp. 5177–5180.

[216] M. Martin-Neira, S. D'Addio, C. Buck, N. Floury, and R. Prieto-Cerdeira, "The PARIS ocean altimeter in-orbit demonstrator," *IEEE Trans. Geosci. Remote Sens.*, vol. 49, no. 6, pp. 2209–2237, Jun. 2011.